Chapter 8
Quantitative Texture Analysis of Polycrystalline Ferroelectrics

D. Chateigner[1], J. Ricote[2]

8.1 Introduction

A large number of physical properties in most crystals are anisotropic. This is even more important in polar materials, like ferroelectrics, where the polarization determines their behaviour. In polycrystals, researchers have developed techniques to grow crystals along preferential orientations and take advantage of the highest values of the anisotropic properties. The preparation of ferroelectric materials with preferential crystallographic orientations, or textures, is useful in obtaining ferroelectric materials with improved properties for a variety of technological applications, like Non-Volatile Ferroelectric Random Access Memories (FeRAMs) [1, 2], where we use the polarization vector for the 0 and 1 bits, or MicroElectroMechanical Systems (MEMS) [3], where the highest piezoelectric coefficients are associated to specific crystallographic directions. Strong textures along polar axis directions perpendicular to the film surface have been sought in ferroelectric thin films as it improves the final response. But sometimes other orientations are also interesting. For example, in lead titanate-based compositions, while orientations along the <001> polar axis are preferred for pyroelectric applications, <111>-oriented films are more desirable for memory applications, because it provides high remnant polarization and abrupt switching behaviour [4]. Preparation routes have been optimized to obtain highly oriented ferroelectric films [5, 6, 7]. As a consequence of all this, interest on texturing of ferroelectric polycrystalline mate-

[1] Laboratoire de CRIstallographie et Science de MATériaux CRISMAT-ENSICAEN, Institut Universitaire de Technologie (IUT), Université de Caen Basse Normandie, 6 Boulevard du Maréchal Juin, F-14050 Caen, France. Phone: +33(0)231452611
FAX: +33(0)231951600
daniel.chateigner@ensicaen.fr
[2] Instituto de Ciencia de Materiales de Madrid, CSIC, C/ Sor Juana Inés de la Cruz 3, Cantoblanco, E-28049 Madrid, Spain
jricote@icmm.csic.es

rials, the quantitative characterization of texture becomes crucial for polycrystalline ferroelectrics. Different techniques are used, and among them, X-ray diffraction has routinely been used as a non-destructive characterization of texture, strain state, particle size, crystal structure and microstructure in general. However, when applied to anisotropic polycrystalline samples, the conventional diffraction approaches generally fail. For instance, a usual Bragg-Brentano diffraction diagram may not reveal all diffracted lines of a compound when it is strongly textured. This makes its structural determination impossible, which in turn impedes reliable quantitative texture analysis. Also, the presence of strongly overlapping diffraction peaks often makes this difficult analysis. This is usually the case of thin films, where diffraction peaks coming from the substrate may become a serious problem to study the structural characteristics of the film. This may be in some cases poorly understood beforehand. Advanced methods of analysis were therefore needed.

In this chapter, we review the various methodologies to analyze the texture of polycrystalline ferroelectrics by X-ray diffraction. A broad range of techniques are offered to the non-specialist: from the conventional scans with poor quantification in terms of textures, to the most advanced techniques of analysis that allow the simultaneous determination of several structural, textural and microsctructural parameters, the so-called combined analysis. We show that the quantitative characterization of textures is possible in complex ferroelectric multiphase materials in thin film form with a series of examples at the end of the chapter.

8.2 Conventional Texture Analysis

Most natural and artificial solids (rocks, ceramics, metals, alloys...) are constituted by aggregates of grains of different phases, sizes, shapes, stress states and orientations. Grains may be viewed at different scales, depending on the technique used to examine them. Using optical microscopes, grains at the micrometer scale are visible, delimited by regions with different characteristics regarding the reflection or transmission of light. Since visible light is in the micrometer wavelength range, the resolution is of the same order, and, therefore, no direct information about the crystal planes is accessible. Only when there is a relationship between the reflection index and the shape of the crystal with the crystallographic plane, may optical microscopy be used to study crystallographic textures. These methods were used by geologists and metallurgists to study texturing effects before they had access to more sophisticated techniques. With the development of Scanning and Transmission Electron Microscopes, studies down to few nanometres were available. Diffraction of electrons, with lower wavelength, by the material is carried out by examining Kikuchi patterns (Electron Backscattered Scanning Diffraction, EBSD) or Debye-Scherrer electron diffraction patterns in TEM, so the crystallographic orientation of the individual crystals can be analyzed [8].

Diffraction using X-rays or neutrons, which have wavelengths comparable to the distances of crystallographic planes, is used for routine determination of texture. It should be noted that X-ray and neutron diffraction probe crystallites and not grains. This is an important issue to take into account when studying polycrystalline materials, as it may lead to misinterpretation of the results. A crystallite is the largest domain that satisfies the periodic translation of the crystal unit-cell in the three dimensional space. The incident radiation is then coherently scattered in one crystallite, which is then called "coherent scattering domain". But grains can be made of a lot of crystallites, overall in ferroelectrics where regions corresponding to different ferroelectric domains are present. Although both terms, grain and crystallite, are often used indistinctively, it is not correct in most cases.

Before going into detailed description of the textures of ferroelectric polycrystals, we need to introduce the basics of the conventional texture analysis based on diffraction. Firstly, the limitations of the normal θ-2θ diffraction diagrams and rocking curves used for routine texture determination will be described. Secondly, pole figures will be introduced as the best method to obtain a more complete picture of textures of materials.

8.2.1 Qualitative Determination of Texture from Conventional Diffraction Diagrams

8.2.1.1 Bragg-Brentano Diagrams

Fig. 8.1 shows the conventional diffraction arrangement used for powder diffraction. It is generally known as the Bragg-Brentano configuration [9]. The incident and diffracted beams define the incident plane (scattering plane), in which diffraction is measured with a scattering vector $\mathbf{\Delta k}$. The detector is placed at an angle 2θ from the incident beam, itself at θ from the sample surface. Using this geometry, crystallographic planes {hkl} of different d-spacing are successively brought into diffraction for different θ. Diffraction by sets of planes not parallel to the sample surface {hkl}' is not collected. Therefore, the information obtained may represent only a low percentage of the volume of the material.

Fig. 8.2 shows Bragg-Brentano diffraction diagrams corresponding to α-SiO_2, from a randomly oriented powder (Fig. 8.2a), and from a material with a strong orientation with {00ℓ} planes parallel to the sample surface (Fig. 8.2b). The latter only exhibits the 003 peak, while it is barely visible in the former. As a result, no information can be obtained about other crystal planes, e.g., {h00}, in the oriented sample. Therefore, the texture may only be characterized qualitatively in this case. Even if the diagram had showed diffraction peaks from other planes, it would be only from planes parallel to the sample plane, not giving information about in-plane preferential orientation of the material.

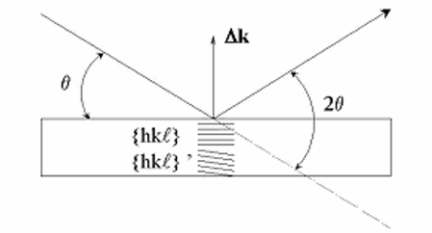

Fig. 8.1 Bragg-Brentano geometry used for diffraction. The plane of the figure is the scattering plane.

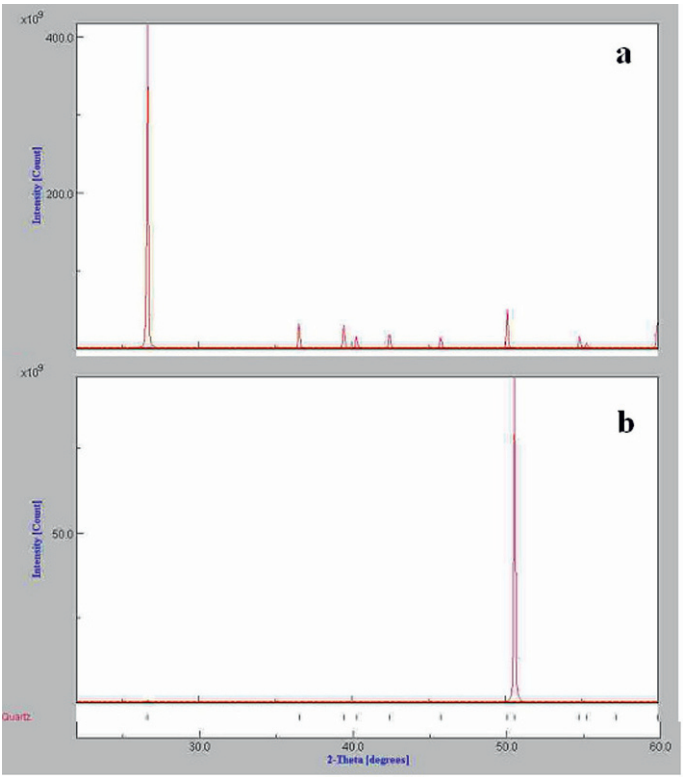

Fig. 8.2 Bragg-Brentano diffraction diagrams of α-SiO_2 for **a** a bulk powder without any preferred orientation and **b** an oriented powder showing strong orientation with {00ℓ} planes parallel to the sample surface.

With this geometry, the available range of observed diffraction peaks may be restricted by construction. Normally, ranges of at best 2θ = 165° are measured. In this range, a randomly oriented sample of the diamond structure (Fd3m space group, a = 3.566 Å) using Cr Kα1 radiation (2.2897 Å) will show only two peaks (Fig. 8.3), corresponding to the {111} and {220} planes. If this sample is instead strongly oriented with {100} planes parallel to the surface of the sample, no diffraction peak will be observed in a Bragg-Brentano diffraction diagram.

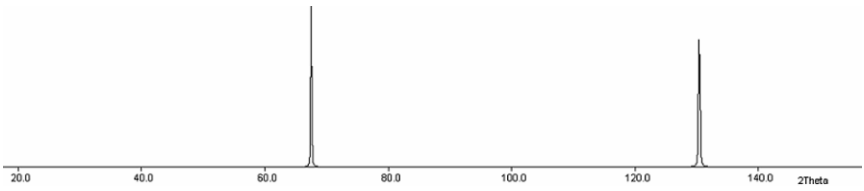

Fig. 8.3 Bragg-Brentano diffraction diagram in the 20-165° 2θ-range, for diamond measured with Cr $K\alpha_1$ radiation.

Regarding in-plane orientations in the sample, Fig. 8.4 shows that for a given {hkℓ} plane family, any rotation around the sample normal, **n**, does not change the diffraction diagram. If {hkℓ} are parallel to the surface, the diffracted intensity is kept constant, while for {hkℓ}' planes (Fig. 8.1) no intensity is detected. Both texture components in Fig. 8.4. have the **c** axes of the structure parallel to **n**, but **a** axes are different, rotated around **n**. We may conclude from this that with this configuration it is impossible to check for eventual in-plane alignment of the axes, like the ones involved in epitaxial growth, for example.

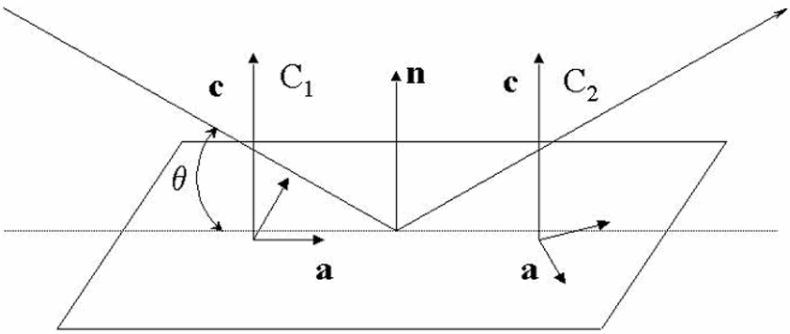

Fig. 8.4 Two texture components differing only by their orientation in the sample plane.

8.2.1.2 Asymmetric Diagrams

The asymmetric configurations for diffraction may be carried out either with a point detector, using an incidence angle ω that is not equal to θ (Fig. 8.5) or with linear and curved position sensitive detectors, PSD [10, 11] (Fig. 8.6). The advantage of PSD is that, while point detectors only probe {hkℓ}' planes that are inclined by δ = ω-θ from the sample plane, they collect information for other sets of planes. In both cases only qualitative characterization of texture is possible, as with the Bragg-Brentano geometry.

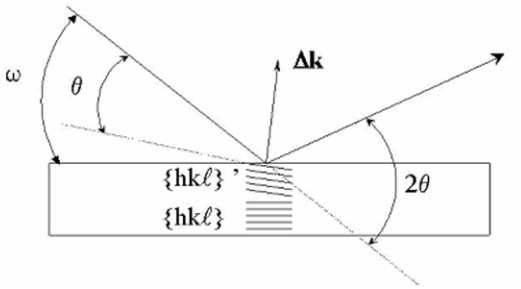

Fig. 8.5 Asymmetric geometry for diffraction with a point detector

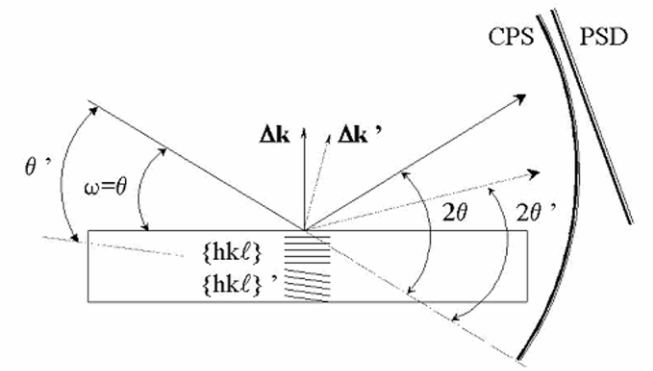

Fig. 8.6 Asymmetric geometry for diffraction with a linear position sensitive detector (PSD) or curved position sensitive detector (CPS).

Regarding in-plane orientations, rotation around **n** of the crystallographic axes will provide some information in the asymmetric configurations, since this rotation will bring to diffract planes, which are not coplanar (except if ω = θ, which corresponds to the regular θ-2θ scan).

8.2.1.3 ω-Scans: Rocking Curves

The ω–scans, also called rocking curve, are often used to reveal the preferential orientation of specific crystallographic planes with respect to the sample surface. For a fixed θ-2θ position, different sets of planes with the same interplanar distances are brought to diffraction by varying ω (Fig. 8.7). This kind of measurement is used to check the quality of as-grown single crystals, obtaining information about their mosaic spread. This method is also used more to measure the texture of thin structures, like ferroelectric films [12], although the mosaicity is then much larger, and often not suited for such a characterization.

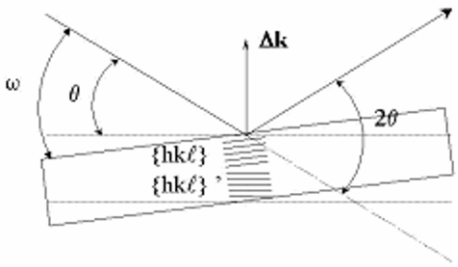

Fig. 8.7 ω-scan (rocking curves) configuration.

A typical rocking curve of a {002} line measured for a single crystal is presented in Fig. 8.8. The FWHM of the curve shown is 0.1° in ω, which means that a certain amount of crystallites are inclined by 0.1° or less with respect to the sample surface. The volume percentage of oriented crystals may also be obtained, and it depends on the curve shape. In this example the curves fits a Gaussian, and approximately 86 % of the intensity is within the FWHM. This means that approximately this is the percentage of oriented crystals in the material.

With this configuration only planes perpendicular to the incident plane can be brought to diffraction. Planes parallel to the scattering plane will never satisfy the Bragg law when rotating around ω (Fig. 8.9).

Rocking curves can produce quantitative information on texture, provided another axis of rotation is added. However, this method suffers from a lack of extent of the available measurements. If we consider a distribution of crystallites well represented by a Gaussian shape with a FWHM of 30°, to bring a plane which makes an angle of ω=-30° with the sample surface into diffraction conditions, one has to rotate the sample by 30°, means ω=θ + 30. In the mean time, if the peak of interest is diffracting at a θ position lower than 30°, the diffracted beam is then fully absorbed in the sample. In this geometry, measurements are limited by the necessary condition ω<± θ. Since Bragg angles for intense peaks (reliable peaks) are located at rather low θ ranges, this limit is far below the necessary ranges of

texture measurements. It is of course suited for low angle ranges and, therefore, for single crystals.

Now consider a distribution of crystallite orientations that is not symmetric around **n** (Fig. 8.10). For instance, composed of two orientations with 0.1° FWHMs, one along **n** (with $\mathbf{c_1}$ axes), the other ($\mathbf{c_2}$ axes) at an angle χ from **n** and φ from the intersection of the sample surface and the scattering plane. Measured as positioned in Fig. 8.10, a rocking curve on $\{00\ell\}$ planes will exhibit only one orientation component, C_1, the only one having $\{00\ell\}$ planes perpendicular to the scattering plane (Fig. 8.8). The C_2 component will be revealed on a $\{00\ell\}$ rocking curve if the sample is rotated by φ around **n** before measurement (Fig. 8.11).

We conclude that ω-scans may reveal the texture of a sample, with the absorption limitations discussed above, if several of these scans are measured in different φ orientations of the sample.

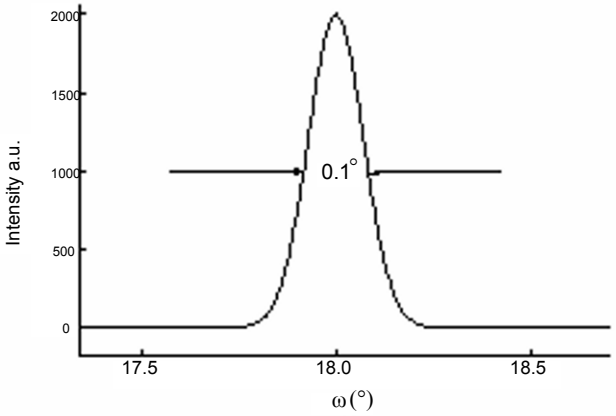

Fig. 8.8 ω-scan of a single crystal having a 0.1° FWHM of its {002} reflection.

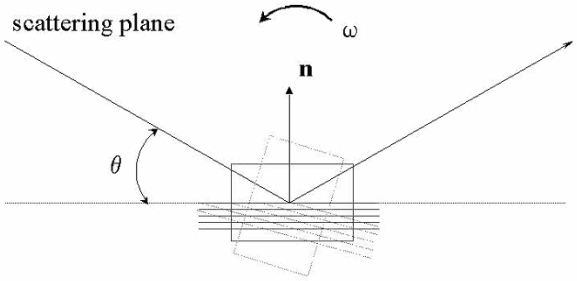

Fig. 8.9 Illustration of crystallographic planes rotation when planes are perpendicular (dotted or continuous lines) or parallel (rectangles) to the diffraction plane.

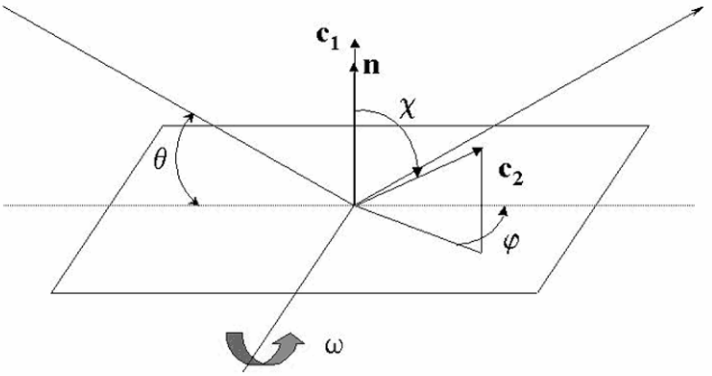

Fig. 8.10 Representation of two orientation components (C_1 and C_2), represented by their c axes.

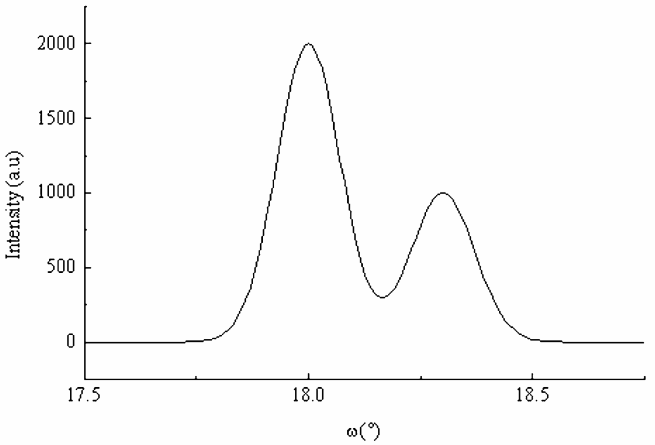

Fig. 8.11 Rocking curves corresponding to the two orientation components as described in Fig. 8.10 after rotation of the sample by φ.

8.2.2 A Quantitative Approach: The Lotgering Factor

Semi-quantitative approaches to determine texture from conventional Bragg-Brentano θ-2θ diffraction diagrams have been developed. The relative ratios of the intensities of the diffraction peaks obtained for a textured material provide information on texture. Lotgering in 1959 [13] derived a quantitative factor, $L_{hk\ell}$, to quantify the degree of orientation of a given material. This factor is defined for a hkℓ orientation by:

$$L_{hk\ell} = \frac{p - p_0}{1 - p_0} \tag{1}$$

where the p factors are obtained from the diffraction diagram of the textured sample (p) and from the diagram of an equivalent sample with random orientation (p_0), and are defined by:

$$p = \frac{\sum_i I\{hk\ell\}_i}{\sum_{hk\ell} I\{hk\ell\}} \tag{2}$$

being $I\{hk\ell\}$ the intensities of the diffraction peaks within a specified 2θ range. p values can vary from p_0 (random oriented sample) to 1 (ideally oriented sample). Therefore, the Lotgering factor may vary from 0 to 1. The higher the value obtained, the more oriented the sample for that direction.

However, if this factor is somehow linked to the texture strength (and Lotgering specifically advised it), this is specific to one set of crystallographic planes. If two or more texture components are present at the same time, several factors must be calculated, with *a priori* no clear relationship between them. We should also be aware that this factor is affected by the θ range chosen for the calculations: the values of the coefficient may vary from 7 to 73% in the same sample depending on the number of reflections used in the calculations [14]. Again, no information can be obtained for in-plane orientation components. Furthermore, the Lotgering factor will be unaffected by the dispersion of the texture components, which is relevant for the correlation of texture results with the physical properties of the material. Therefore, it must be considered as a qualitative factor that may lead to false conclusions when used without taking into account its limitations.

8.2.3 Approaches to Texture Characterization Based on Rietveld Analysis

Preferred orientations have been considered for long in Rietveld analysis as an undesired phenomenon. Many techniques have been described to remove texturing effect prior or during measurements. However, quantitative texture analysis may be included in the Rietveld analysis. To do that, texture can be described using three parameters:

1. The Texturing Direction in the Sample
2. The Crystallographic Direction **h** that is Aligned Preferentially along the Texturing Direction
3. The Texture Strength (the Degree of Orientation and the Angular Dispersion)

The original March approach includes the preferred orientations in the Rietveld equation using the function $P_{\mathbf{h}}$:

$$P_{\mathbf{h}} = G_2 + (1 - G_1)\exp(-G_1\alpha_{\mathbf{h}}^2) \tag{3}$$

being G_1 and G_2 refinable parameters and $\alpha_{\mathbf{h}}$ the angle between the crystallographic direction **h** and the scattering vector **Δk**.

Later, Dollase modified the function:

$$P_{\mathbf{h}} = (G_1^2 \cos^2 \alpha_{\mathbf{h}} + \left(\frac{1}{G_1}\right)\sin^2 \alpha_{\mathbf{h}})^{-3/2} \tag{4}$$

Originally, the correction assumed a Gaussian distribution of the preferred orientation axis of the individual crystallites about the normal to the sample surface. G_1 is the refinable parameter ($G_1 = 1$ means no preferred orientation) that controls the distribution shape. It is an estimate of the preferred orientation strength. The model provides:

- a preferred orientation correction factor that is minimum or maximum at $\alpha = 0°$
- a symmetric and smooth evolution in the [0,90°] $\alpha_{\mathbf{h}}$ range
- a single parameter to be fitted
- the possibility of normalization of the orientation with

$$\int_0^{\frac{\pi}{2}} P_{\mathbf{h}} d\alpha = 1$$

The normalization is important in order to keep constant the total diffracted intensity in a diffraction diagram whatever the distribution shape $P_{\mathbf{h}}$.

More recently, a modification of the March-Dollase approach was proposed [15]:

$$P_{\mathbf{h}} = f\left\{(G_1^2 \cos^2 \alpha_{\mathbf{h}} + \left(\frac{1}{G_1}\right)\sin^2 \alpha_{\mathbf{h}})^{-3/2}\right\} + (1 - f) \tag{5}$$

In this formulation, it is expected that the factor f allows the inclusion of the randomly oriented part of crystallites (in volume). However, it must be noted that this factor is linked to the component of orientation that is described by the formula. This latter only describes one orientation component, i.e., a specific **h** distributed around the perpendicular direction to the sample surface. Therefore, f is only the volume fraction of crystallites that do have their **h** direction in this distribution component, (1-f) being the volume fraction of crystallites that are oriented differently, but not necessarily randomly oriented. To illustrate this point, we will

give an example: imagine a sample containing tetragonal crystallites with a single orientation component, e.g., with their c-axes distributed around the normal to the sample surface. In this case, if f=0.5, 50% of the crystallites must have [001] directions among those included in that distribution. However, nothing is said for instance about the orientation of a-axes around the orientation component. Therefore, we cannot conclude that the 50% crystallites remaining are necessarily randomly oriented. As a conclusion, the parameter f does not represent the orientation distribution function in equation 5.

In all these calculations, it is always assumed there is only one component in texture and that directions are axially distributed (with a cylindrical symmetry around the scattering vector for a Bragg-Brentano geometry). The approach proved to be efficient for these conditions [16, 17, 18]. It is implemented in many software programs for diffraction analysis, and some of them allow a bi-texture component of this type. For all the other textures, measurements and formalisms to resolve the texture are more complex and have to be adapted for each case. This is unless a destruction of the sample is acceptable, as has been demonstrated for instance by O'Connor *et al.* [19]. Furthermore, the geometry used for the measurements plays an important role. The previous expressions describe the orientations with respect to the sample reference frame, while measurements are carried out in the spectrometer frame. The relationships between the two frames are straightforward when using conventional Bragg-Brentano geometry, but not for other geometries, like rocking curves. It requires, therefore, a localization correction that relates plane normal in the sample frame.

None of these approaches allow the description of textures in terms of distribution densities, due to a lack of normalization of texture results. Therefore, they depend on material characteristics that vary from one to another like porosity, crystalline state...

Another approach is the so-called arbitrary texture correction. This is not a model, and as such cannot be interpreted in terms of physically understandable parameters of texture. It only deserves the fitting possibility of diagrams that show textures, but ones that are not of interest or that cannot be measured (*e.g.* if not enough data have been acquired for this purpose). The correction simply consists in assigning arbitrary intensity values to the peaks in order that it respects observations. Whenever no texture correction would produce a satisfactory fit, one may use this correction to obtain a better fit of the observed intensities. This will allow obtaining more reliable cell parameters to start the analysis.

8.2.4 Representations of Textures: Pole Figures

8.2.4.1 Pole Spheres and Pole Figures

Fig. 8.12 represents a single crystallite orientation with the **c** axis at χ from **n**, and at φ from the macroscopic edges of the sample. The sphere on which all orientations can be distributed is also shown. This sphere of unit radius is called the Pole Sphere, with a $4\pi^2$ surface. The orientations may then be distributed over a solid angle of $4\pi^2$ sr at maximum. The intersection of the crystallographic direction [hkℓ] with the surface of the Pole Sphere is called a "pole", for instance the south or north poles. In these representations, we are interested in the {hkℓ} planes distribution. We choose to locate the orientation of one (hkℓ) plane by its normal [hkℓ]*. Consequently, all {hkℓ} planes will be located by their respective <hkℓ>* directions.

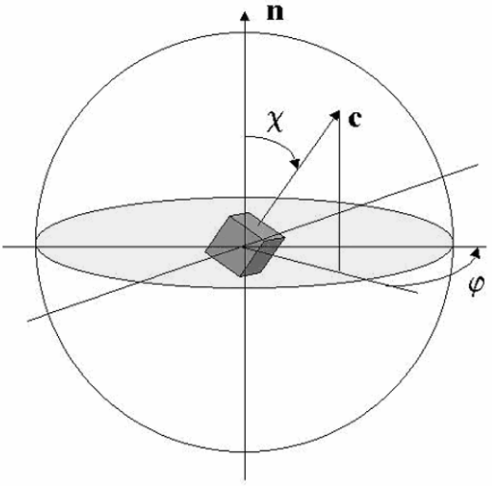

Fig. 8.12 Representation of a crystallite orientation on the Pole Sphere.

A Pole Sphere of a polycrystal will be the representation of all the poles of all the crystallites of the sample. For cubic crystal structures, for which [hkℓ] $\perp$ {hkℓ}, the interpretation of the Pole Sphere is then straightforward. But for any other crystal system this relationship is not generally valid, and we may need the help of the reciprocal lattice construction. As evidence, plotting all the poles of all the {hkℓ} planes of all the crystallites of a sample would rapidly tend to a perfect homogeneous coverage of the Pole Sphere. Interesting information will be visible if we represent the poles for only one family of {hkℓ} planes. We will call this a

{hkℓ} Pole Sphere. Also experimentally several {hkℓ} plane families may not be separated, and we will have then a {hkℓ/h'k'ℓ'} Multipole Sphere.

One entity that will be used is the unit surface element of the Pole Sphere, dS, the surface drawn for a (dχ, dφ) elementary variation. For the pole sphere of unit radius, this elementary surface is:

$$dS = \sin\chi \, d\chi \, d\varphi \tag{6}$$

It is not easy to represent a three dimensional object like a Pole Sphere and, although some programs can do it, to interpret them this way. Interpreting the Pole Sphere using two-dimensional projections is by far easier. We will call these projections {hkℓ} pole figures. Fig. 8.13a shows the stereographic projection of the pole sphere in the case of the single pole of Fig. 8.12. A pole, P, representing the intersection of [hkℓ]* with the Pole Sphere, is projected on the equatorial plane in p, intersection of SP with the equatorial plane. In this projection, the φ angle is conserved. All points located at the same φ are describing a meridian (large circle) and all points at the same χ are at the same latitude (on a small circle). Hence, a pole P(χ,φ) of the Pole Sphere is represented by the pole p(r',φ) in the {hkℓ} pole figure, where r' is the distance Op. Since r = R sinχ, we can plot a pole figure with any radius R using:

$$r' = R \tan(\chi/2) \tag{7}$$

In such a projection, since tanχ is increasing with χ, two points located at the same angular distance Δχ on the sphere will be farther from one another near the periphery of the projection than near its centre (Fig. 8.13a). Then, randomly distributed points on the sphere will appear more concentrated in the centre of the projection. Also, the surface element (surface between four adjacent points) is larger for larger χ's. Wulff nets (Fig 8.13b) may be used to manually determine angles between directions or planes on such projections.

Another type of projection is the Lambert or equal area projection. The pole P(χ,φ) is projected on the plane tangent to the Pole Sphere containing the north pole (Fig. 8.14), which is also conserving the φ angle. The rotation is around an axis perpendicular to the φ meridian passing by O, centre of the projection. The relation Op = OP is then valid for all points of the projection. For instance, a pole of the equator (χ = 90°) will be at R√2 from O in the projection. The projection p(r',φ) can be obtained whatever R by:

$$r' = 2R \sin(\chi/2) \tag{8}$$

For a given increase in χ, the distance between two points of the projection will decrease slowly, particularly in the high χ-range. This decrease will partially compensate the increase in surface element due to φ. Then this surface element will be similar near the periphery and near the centre of the projection (Fig. 8.15b), which is why this projection type is called "equal-area". Schmidt nets may be used to manually determine angles between directions or planes on this type of projections.

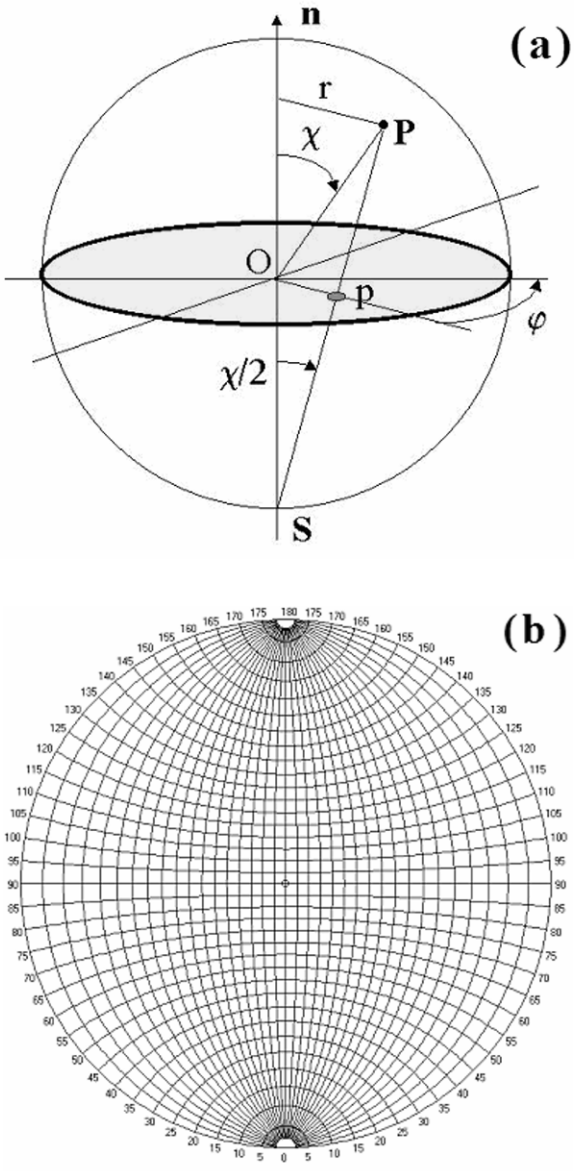

Fig. 8.13a Stereographic projection of figure 12 and **b** Wulff net to manually read angles in the projection

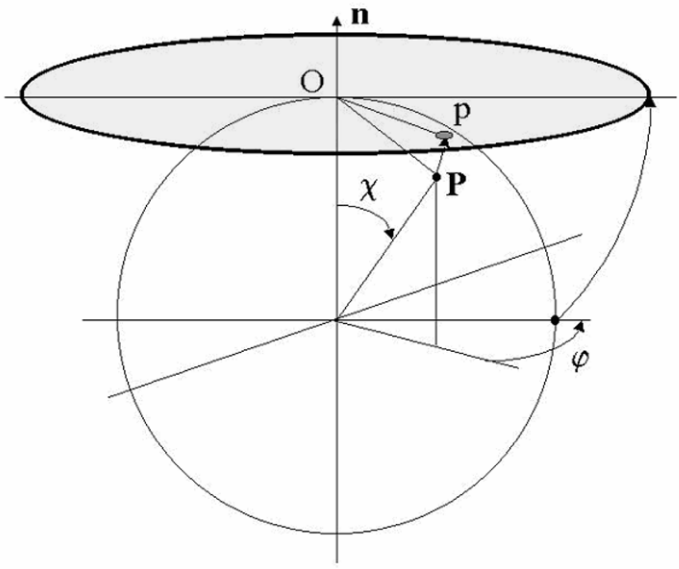

Fig. 8.14 Lambert projection of Fig. 8.12.

A value of the intensity $I_{hkl}(\chi,\varphi)$ is associated to each point of a {hkℓ} pole figure. Depending on the geometry of the experimental set-up, the angles χ and φ used in the diffractometer may need to be converted to get the real pole figures. In all the following, χ and φ will correspond to the ones of the diffractometer (spectrometer) space *S*. After corrections, the angles retrieved in the pole figures space, *Y*, will be ϑ_y and φ_y, or simply $\mathbf{y}=(\vartheta_y,\varphi_y)$. Similarly, since pole figures will represent <hkℓ>* direction distributions, we will simplify the notation into $\mathbf{h}$=<hkℓ>*. Hence, the diffracted intensities represented on a Direct Pole Figure will be called $I_{\mathbf{h}}(\mathbf{y})$.

Since diffraction is depending on the density of the material (porosity, density of the phase in a polyphased material …), crystalline ratio (polymers …), thickness (thin films, multilayer …), diffraction yields (different planes diffract different intensities), particle sizes, stress/strain states …, comparison among the orientation distributions obtained from pole figures of different samples becomes impossible. We then have to normalize these intensities into pole densities, or distribution densities, $P_{\mathbf{h}}(\mathbf{y})$. The resulting pole figures will be called Normalized Pole Figures. While direct pole figures are showing diffracted intensities, in diffracted counts, the unit of normalized poles is the multiple of a random distribution, or m.r.d.. Using these units, a sample without a preferred orientation will exhibit normalized pole figures with 1 m.r.d. for all $\mathbf{h}$ and $\mathbf{y}$'s, i.e., $P_{\mathbf{h}}(\mathbf{y}) = 1$ m.r.d.. A textured sample will show minima and maxima of densities, the minimum attainable density being 0.

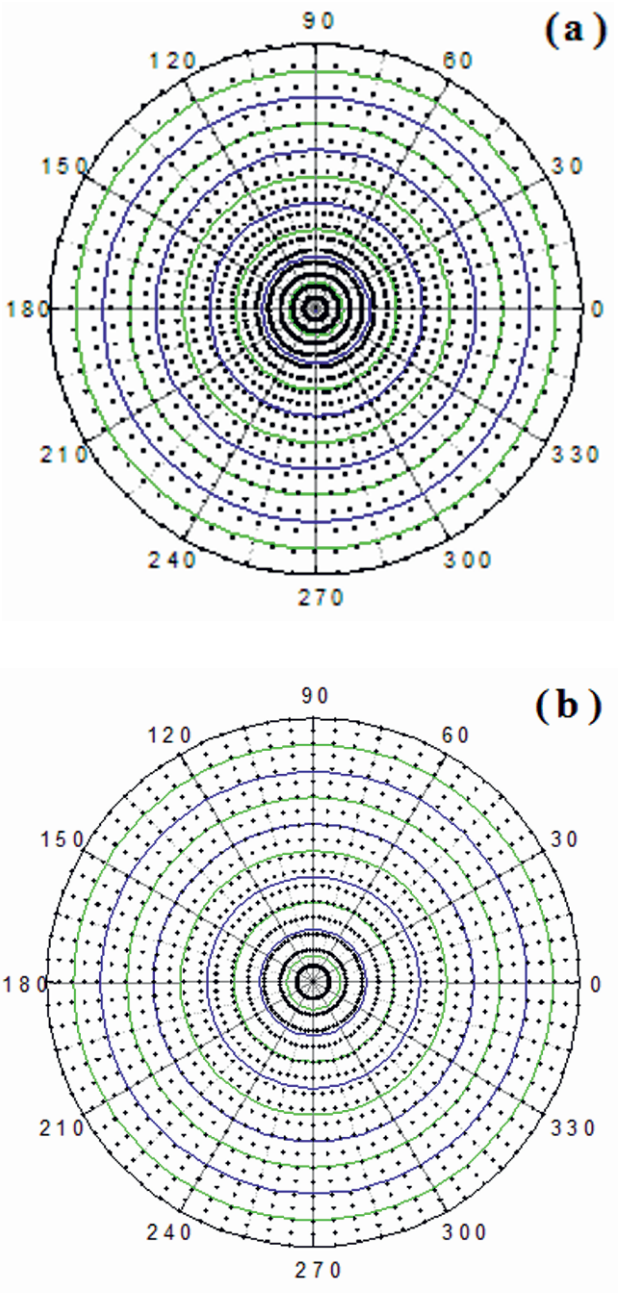

Fig. 8.15a Stereographic and **b** equal-area projections of 1368 points located at every 5° in χ and φ on the Pole Sphere.

8.2.4.2 Analysis of Direct Pole Figures

Pole figures are representations of the distributions of crystalline directions, as measured by diffraction. In normal conditions for diffraction, i.e., far enough from the atomic absorption edges, (hkℓ) and ($\bar{h}\ \bar{k}\ \bar{\ell}$) planes are diffracting the same intensities (Friedel's law), at the same Bragg angle. It is then not useful to measure or represent the whole Pole Sphere, and only half of it, the upper hemisphere, will be considered. Of interest is the location of specific **h**'s in the sample that we are measuring. We need to associate them with the sample a reference frame, which will be used in the pole figures. This sample reference frame, K_A, is made of three unit-vectors ($\mathbf{x_A}$,$\mathbf{y_A}$,$\mathbf{z_A}$) of the respective axes, X_A, Y_A, Z_A, such that $\mathbf{x_A} \wedge \mathbf{y_A} = \mathbf{z_A}$ (Fig. 8.16). In order to simplify, we generally try to align these axes with macroscopic features of the sample. For instance, Z_A is positioned parallel to **n**, and the two other axes with the edges of the sample. The scattering plane is then perpendicular to (X_A,Y_A) in conventional diffractometers. In K_A, a vector will be represented by its coordinates in terms of the unit-vectors ($\mathbf{x_A}$,$\mathbf{y_A}$,$\mathbf{z_A}$). For instance, the Z_A axis is co-linear to the vector **[001]** of the sample frame K_A. Note that the **[XYZ]** coordinates are bold characters; they have no correlation with the Miller indices which indicate crystal-related quantities.

Inside the sample are crystallites, having their own reference frame, K_B, with their own unit-vectors ($\mathbf{x_B}$,$\mathbf{y_B}$,$\mathbf{z_B}$) and axes, X_B, Y_B, Z_B (Fig. 8.17). Similarly, we fix the normal to the diffracting plane of the crystallite, [hkℓ]*, parallel to Z_B. For crystal structures with right angles of the unit-cell (cubic, tetragonal and orthorhombic), X_B, Y_B, Z_B may be chosen parallel to **a**, **b**, **c** respectively, both frames having equal unit-vectors. However for other crystal systems, this is no longer the case, and the crystal structure will be needed to know the correspondence between K_B and **a**, **b**, **c**.

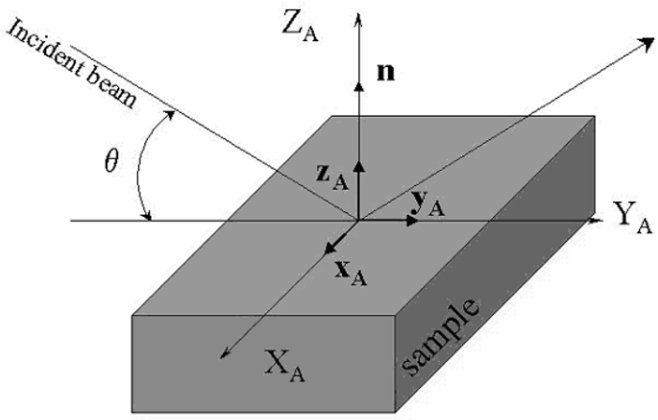

Fig. 8.16 The sample reference frame $K_A = (x_A, y_A, z_A)$.

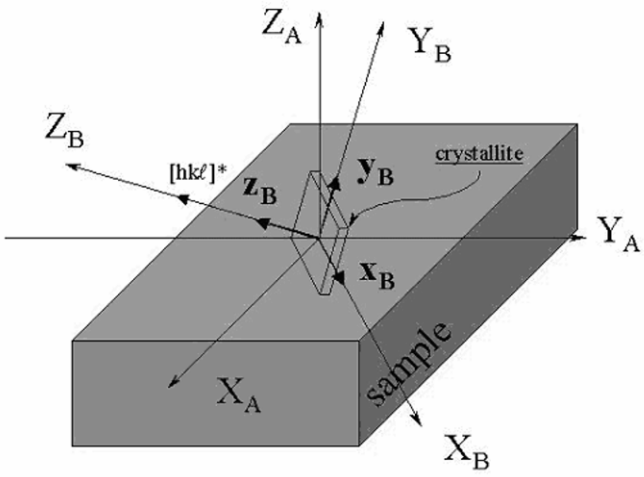

Fig. 8.17 Crystal and sample reference frames $K_B = (\mathbf{x_B}, \mathbf{y_B}, \mathbf{z_B})$ and K_A respectively. Only one crystallite is shown.

In order to represent the textures, we will then use K_B and K_A in the pole figures. The pole figures will be represented in such a way that Z_A is their normal axis, X_A the horizontal axis and Y_A the vertical axis (Fig. 8.18). For one crystallite (Fig. 8.18a), a direction **y** associated to the normal [hkℓ]* of the diffracting plane (hkℓ), is then localized by the polar angle ϑ_y and the azimuth angle φ_y. This latter takes its origin along X_A, and is taken positive for a left-handed rotation when looking down Z_A. It then respects the mathematical definition of K_A for a direct reference frame.

However, in a polycrystal, a large number of crystallites are diffracting, and the pole figure shows regions with large diffracted intensities (or densities, if we deal with normalized pole figures), indicating the tendencies of the crystallites to align around a given direction of the sample. The pole drawn by such an ensemble of crystallites (Fig. 8.18b) is called a texture component. For one component, the pole enlarges around the previous **y** direction, meaning that some of the crystallites are about to align with **y**, but not strictly. It is then useful to describe the component by the same ϑ_y and φ_y angles as **y**, but giving the shape of the distribution and a parameter which quantifies how much the pole spreads, for instance Gaussian with 10° FWHM. But we should never forget that describing a pole by an analytical function imposes that we know the distribution is respecting the imposed shape, which is not easily verifiable. For instance, in thin films, poles may appear very much elongated in one direction, but not in the other [20] due to the substrate interaction with the film. Also, distributions may exhibit shapes that are other than Gaussian, Lorentzian for instance [21]. The diffraction intensity (then density) will depend on how the dispersion is for a given pole. The larger the dispersion, the lower the diffraction will be. The intensity and density values are rep-

resented by colour or contour levels. However, for now, we have not normalized the pole figures into quantitative densities, and it is not necessary to indicate these intensity scales.

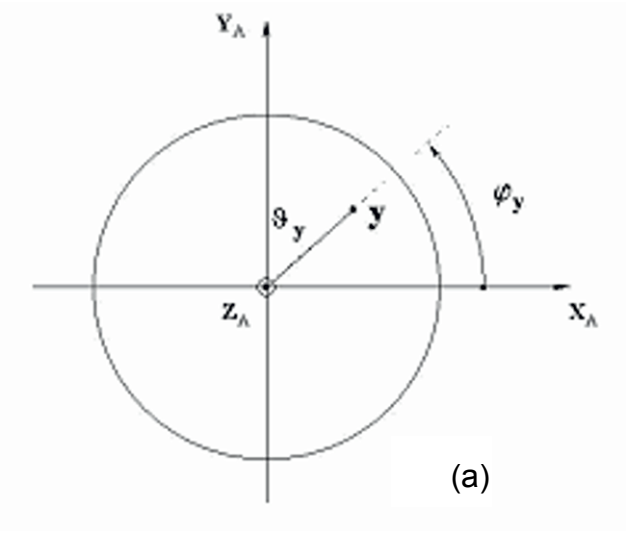

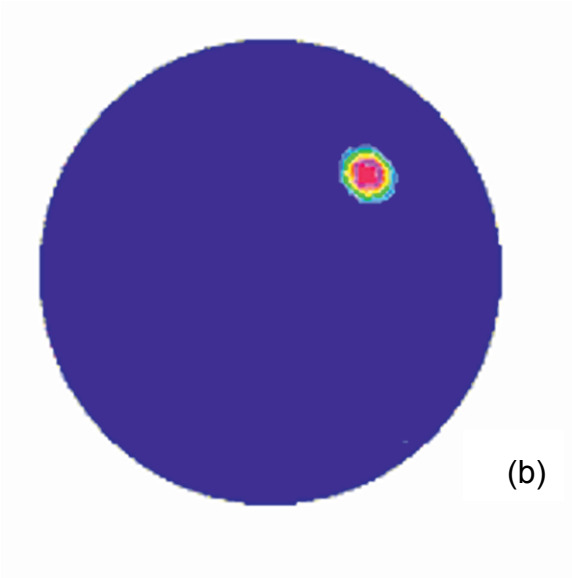

Fig. 8.18a $P_h\mathbf{y}$ Diffraction pole figure for one crystallite. The direction **y** is associated to the [hkℓ]* normal. **b** Pole figure of a texture component centred on the previous **y**, having a Gaussian shape of 10° FWHM, for h = <001>* of an orthorhombic crystal structure.

Using diffraction, all the (hkℓ) diffracting at the same Bragg angle will be found on the same $P_{\mathbf{h}}(\mathbf{y})$ pole figure. For instance, (123) and (321) in a cubic crystal system. Then the pole figure has to also show this multiplicity. Taking the C_1 component of Fig. 8.10 in a cubic structure, a pole figure like the one shown in Fig. 8.19 will be obtained. It can be observed a full pole {001} and four halves (corresponding to {100} and {010}) at 90° in ϑ_y from {001}. The multiplicity of this pole figure is three at total, while the crystallographic multiplicity of the {100} reflection of a cubic crystal system is six. This can be explained due to the fact that we are only concerned with the upper hemisphere of the pole sphere in normal diffraction pole figures.

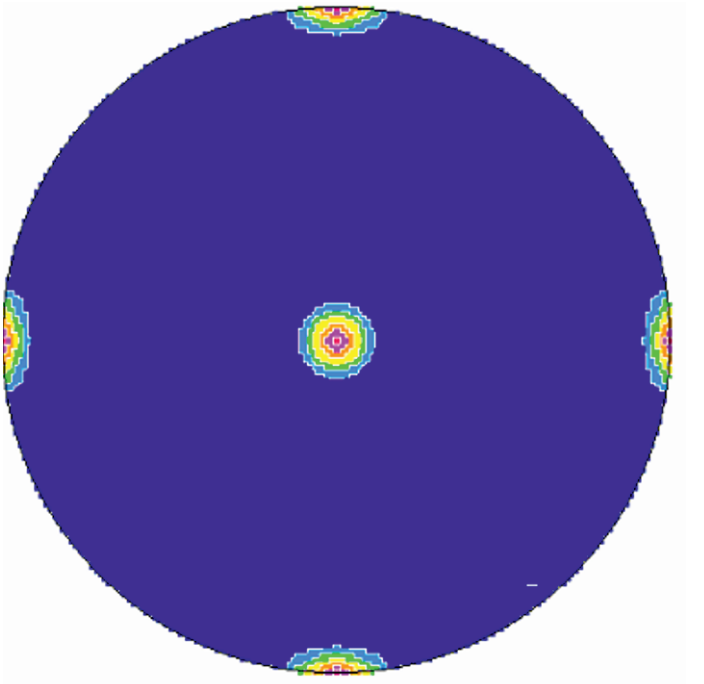

Fig. 8.19 {001} Pole figure for the component C_1 of Figure 8.10, for a cubic crystal structure.

As we have seen in the previous paragraphs, a pole figure can then be a complex object to interpret: it is a combination of a multiplicity, of components, with more or less regular dispersions. Fig. 8.20 shows pole figures that are combining many of these effects. They have been measured on a real sample, an aragonite layer from the sea shell (a cowry) *Cypraea testudinaria.* These pole figures are combining twinning, dispersion and two components, of the orthorhombic crystal system [22]. As it can be seen, pole figures are not easily interpretable, and some tools to relate them to the orientation space are needed.

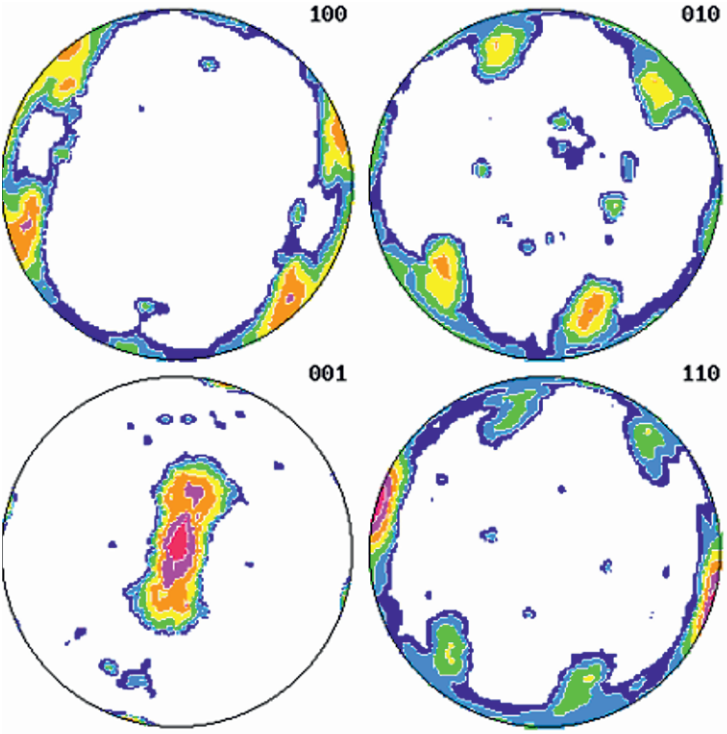

Fig. 8.20 {100}, {010}, {001} and {110} pole figures of an aragonite (orthorhombic crystal system) layer from the sea shell *Cypraea testudinaria*.

8.2.4.3 Pole Figures and Orientation Spaces

Diffraction measurements give in the *Y* space the pole figures, $P_{\mathbf{h}}(\mathbf{y})$ (Fig. 8.18.a), after proper geometrical transformations from the *S* space. They represent the volumetric density of crystallites oriented in **dy**, i.e., between (ϑ_y, φ_y) and (ϑ_y + $d\vartheta_y$, φ_y + φ_y). This can be expressed by:

$$\frac{dV(\mathbf{y})}{V} = \frac{1}{4\pi} P_{\mathbf{h}}(\mathbf{y})\, \mathbf{dy} \tag{9}$$

where V is the irradiated volume of the sample and dV(**y**) the volume of crystallites which orientation is with **h** directions between **y** and **y**+**dy**. Similarly to equation 6 and for consistency we have:

$$\mathbf{dy} = \sin\vartheta_y\, d\vartheta_y\, d\varphi_y \tag{10}$$

and the $1/4\pi$ is a normalization factor to distribution densities of pole figures according to:

$$\int_{\varphi_y=0}^{2\pi}\int_{\vartheta_y=0}^{\pi/2} P_{\mathbf{h}}(\vartheta_y,\varphi_y)\sin\vartheta_y \, d\vartheta_y d\varphi_y = 4\pi \tag{11}$$

The orientation of planes is defined by referring them to at least two directions in the real space. We then need another concept, the Orientation Distribution Function (ODF), f(g). This function represents the statistical distribution of the orientations of the crystallites in a polycrystalline aggregate. It is defined similarly by:

$$\frac{dV(g)}{V} = \frac{1}{8\pi^2} f(g)\, dg \tag{12}$$

where dg = sin(β)dβdαdγ is the orientation element (defined in a 3-dimensional space), defined by three Euler angles, g=α,β,γ in the orientation space (or *G*-space) (Fig. 8.21).

These three Euler angles bring the crystal coordinate system K_B collinear with the sample coordinate system K_A. The *G*-space may be constructed from the space groups, taking into account their rotation parts (since orientations are rotations) and the inversion centre (since we are using normal diffraction). The two first angles α and β determine generally the orientation of the <001>* crystallite directions in K_A, they are called azimuth and co-latitude (or pole distance) respectively. The third angle, γ, defines the location of another crystallographic direction, chosen as <010>* (or **b** in the (**a**,**b**) plane of an orthogonal crystal system). V is the irradiated volume of the sample, dV(g) the volume of crystallites which orientation is between g and g+dg.

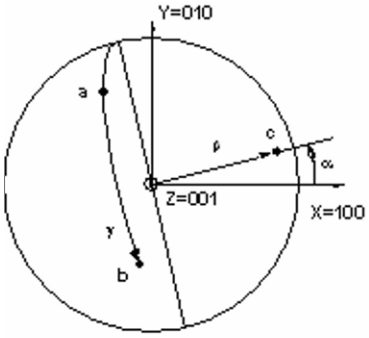

Fig. 8.21 Representation of the three Euler angles that define the position of the crystallite coordinate system K_B of an orthogonal crystal cell in the sample coordinate system K_A. Note, **100**, **010** and **001** are not Miller indices but vectors referring to an ortho-normal frame aligned with K_A.

The function f(g) then represents the volumetric density of crystallites oriented in dg. It is also measured in m.r.d. and normalized to the value $f_r(g)=1$ for a random sample. The normalization condition of f(g) over the whole orientation space is expressed by:

$$\int_{\alpha=0}^{2\pi}\int_{\beta=0}^{\pi/2}\int_{\gamma=0}^{2\pi} f(g)\,dg = 8\pi^2 \tag{13}$$

The function f(g) can take values from 0 (absence of crystallites oriented in dg around g) to infinity (for some of the *G*-space values of single crystals).

From equations (9) and (12) it follows the fundamental equation of texture analysis:

$$P_{\mathbf{h}}(\mathbf{y}) = \frac{1}{2\pi}\int_{\mathbf{h}//\mathbf{y}} f(g)\,d\tilde{\varphi} \tag{14}$$

This equation represents the fact that each pole figure (a 2D object) is a projection along a certain path $\tilde{\varphi}$ of the ODF (a 3D object), which of course depends on the crystal symmetry (Fig. 8.22). Each cell of a given pole figure will then be an average over several cells of the ODF, and each cell of the ODF will be measured by one or more cells from the pole figures. The larger the number of pole figure cells that measure a specific ODF cell, the more statistically reliable is the measurement of this ODF. In practice, one has to measure the largest number as possible of reliable (enough intense) pole figures to define the ODF with the best resolution available.

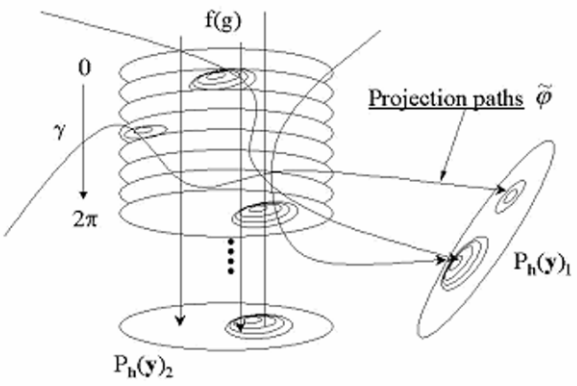

Fig. 8.22 Relationship between the 3D object f(g) and the pole figures $PB_{hB}(y)$. To each pole figure cell correspond several ODF boxes, and each ODF box is linked to several pole figure cells.

Equation (14) was solved several years ago by Bunge, using generalized spherical harmonics formulation [23, 24], but only in the case of high crystal symmetries. An exact solution in an analytical closed form without a series expansion was given [25]. The so-called "vector" [26, 27], entropy maximization [28], component [29] and ADC [30] methods were developed later. The description of these methods is beyond the scope of this chapter. We will describe briefly in the next section how the two main methods used.

The orientation distribution function, which therefore can be calculated from experimental pole figures, provides complete information of all texture components (in-plane and out-of-plane) and allows the calculation of a global degree of orientation. From it we can obtain recalculated direct and normalised pole figures and also the so-called inverse pole figures. They represent the densities of crystalline directions that are parallel to a specific sample direction. Therefore, all texture components along that direction can be visualized directly, and even their relative contributions can be estimated. Several examples of inverse pole figures will be shown in section 5. The objective of the quantitative texture analysis is the calculation of the orientation distribution function.

8.3 Quantitative Texture Analysis

8.3.1 Calculation of the Orientation Distribution Function

To obtain the Orientation Distribution Function is necessary to solve the fundamental equation 14. In the case of the generalized spherical harmonics or the component methods, we obtain a function of the orientation distribution of the crystallites. However, there is no *a priori* need for fitting the experimental data of pole figures to a function, and many “direct” methods (*e.g.* the maximization of entropy, vector or WIMV methods) do not obtain a function. In this case the term "function" can be omitted, and the literature refers to Orientation Distributions (OD). In this respect, since we will only show results from direct methods of f(g) refinements, only "OD" will be used to call f(g). But, even for ODs that have been refined using direct methods, it is somewhat hard to represent ODs on figures without using contour and isolines, which in turn are the result of interpolations of discrete OD points by functions (*e.g.* splines).

8.3.1.1 Williams-Imhof-Matthies-Vinel (WIMV) Method

The WIMV approach [31]- [32 33] for the refinement of the OD is an iterative calculation method based on the numerical refinement of f(g) at step n+1:

$$f^{n+1}(g) = N_n \frac{f^n(g) f^0(g)}{\left(\prod_{\mathbf{h}=1}^{\mathrm{I}} \prod_{m=1}^{M_\mathbf{h}} P_\mathbf{h}^n(\mathbf{y}) \right)^{\frac{1}{IM_\mathbf{h}}}} \tag{15}$$

where the product extends over the I experimentally measured pole figures and for all the poles multiplicity $M_\mathbf{h}$. $f^n(g)$ and $P_\mathbf{h}^n(\mathbf{y})$ represent the refined values of f(g) and $P_\mathbf{h}(\mathbf{y})$ at the n^{th} step respectively. The number N_n is a normalizing factor. The $P_\mathbf{h}^n(\mathbf{y})$ values are calculated at each cycle with equation 15. The first step in this procedure is to evaluate $f^0(g)$:

$$f^0(g) = N_0 \left(\prod_{\mathbf{h}=1}^{\mathrm{I}} \prod_{m=1}^{M_\mathbf{h}} P_\mathbf{h}^{\exp}(\mathbf{y}) \right)^{\frac{1}{IM_\mathbf{h}}} \tag{16}$$

in which $P_\mathbf{h}^{\exp}(\mathbf{y})$ stands for the measured pole figures.

The WIMV algorithm maximizes the so-called "phon" (orientation background or minimum value of the OD which represents the randomly oriented fraction of the sample volume) and the texture sharpness.

The regular WIMV method necessitates an OD divided into a finite number of regular cells. Inside each cell a discrete value of the OD is associated. When the WIMV calculation is inserted inside the Rietveld refinement procedure, it requires two additional steps:

- the extraction of the pole figures or texture weights
- the interpolation of these weights to fit the regular grid

This renders non-optimized values of the OD, particularly for sharp textures and coarse irregular coverage of the OD.

The extended WIMV approach (E-WIMV) can be used with irregular coverage of the OD space and includes smoothing based on a concept similar to the tube projection of the ADC method [30]. The extension of the method uses an iterative scheme of the OD refinement, which is close to the maximization of entropy [34]. The E-WIMV method is then often called Entropy-modified WIMV, and it has been applied to ferroelectric materials [35, 36]. The OD cell values are computed through an entropy iteration algorithm that includes the reflection weights:

$$f^{n+1}(g) = f^n(g) \prod_{m=1}^{M_\mathbf{h}} \left(\frac{P_\mathbf{h}(\mathbf{y})}{P_\mathbf{h}^n(\mathbf{y})} \right)^{r_n \frac{w_\mathbf{h}}{M_\mathbf{h}}} \tag{17}$$

in which r_n is a relaxation parameter such that $0 < r_n < 1$, $M_\mathbf{h}$ is the number of division points for the discretisation of the integral of all the orientations around the scattering vector for the pole figure **h**. The reflection weight $w_\mathbf{h}$ is introduced to

take into account the different accuracy of the more intense and less overlapped reflections with respect to the smaller ones, and is calculated analogously to the weight factors of the Rietveld analysis. The efficiency of this approach has been proved in a series of works [37, 38, 39, 40]. Figure 8.23 shows the results of two refinements using the WIMV and E-WIMV algorithms for the X-ray diagrams measured at $\chi = 0°$ on a Ca-modified $PbTiO_3$ thin film deposited on a $Pt/TiO_2/SiO_2/Si(100)$ substrate [39]. It can be seen that the E-WIMV approach achieves a better refinement, particularly for the sharp peaks of the highly oriented Pt layer.

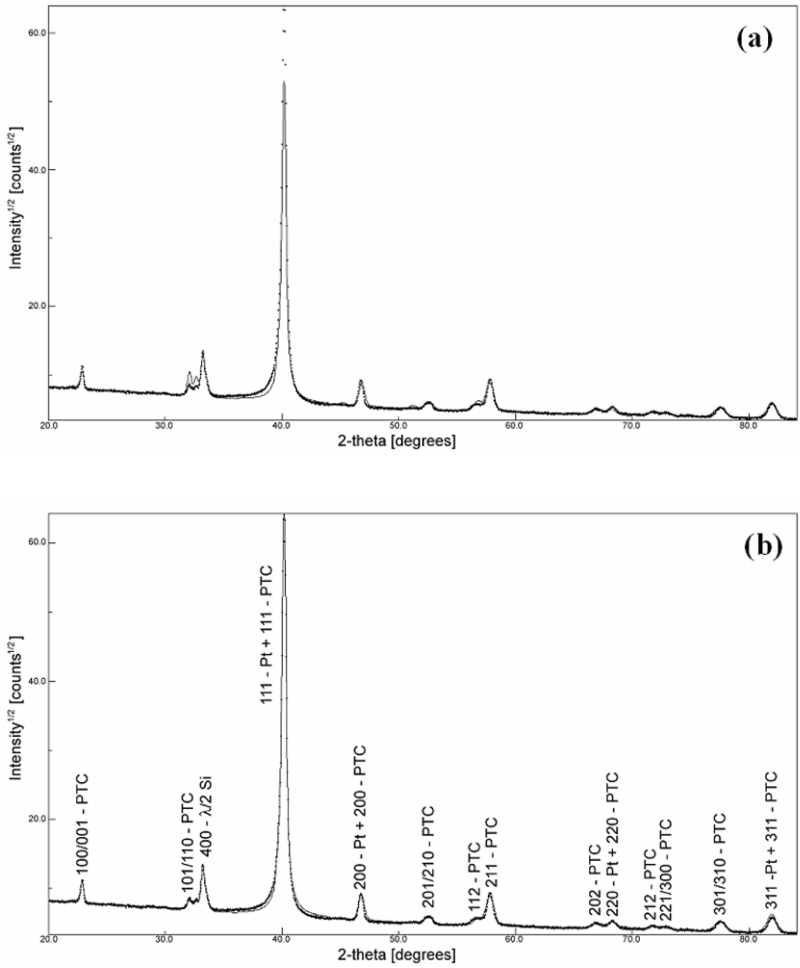

Fig. 8.23 Experimental X-ray diagrams (dotted line) and their corresponding refinement (solid line) using **a** WIMV and **b** E-WIMV approaches.

8.3.1.2 OD Refinement Reliability Factors

The best solution found for f(g) is in most programs given for the minimum averaged reliability factors, RP:

$$\overline{RP_x} = \frac{1}{I}\sum_i \sum_j \frac{\left|P^c_{\mathbf{h}_i}(\mathbf{y}_j) - P^o_{\mathbf{h}_{ii}}(\mathbf{y}_j)\right|}{P^o_{\mathbf{h}_i}(\mathbf{y}_j)} \tag{18}$$

where:

$\mathbf{h}_i$, i = (1..*I*) Measured pole figures
$\mathbf{y}_j$, j = (1..J) Measured points of the pole figures

$\begin{cases} o\text{: observed normalised} \\ c\text{: WIMV-recalculated normalised} \end{cases}$

$P_{\mathbf{h}_i}(\mathbf{y}_j)$ Pole density at $\mathbf{y}_j$ on pole figure $\mathbf{h}_i$

x = 0, ε, 1, 10 ...: criterion to estimate accuracy *versus* density level.

The value x is a criterion used to estimate the quality of the refinement for the low and high-density levels. We use x = 0.05 for the global quality and x = 1 to show this quality for the density values higher than 1 m.r.d.

If the RP factors are suitable for the refinement itself, they depend on the texture strength since they are not weighed by the density level. Consequently, a comparison of the refinement's quality between different samples is somehow ambiguous [40]. In other words, one should compare the refinement quality with RP factors only for materials with similar textures. Furthermore, these factors may depend on the way the OD refinement is obtained (Harmonics, WIMV ...), and also on the grid used for the measurements.

There are several RP factors. The individual relative deviation factors are defined as:

$$RP^z_x(h_i) = \frac{\sum_{j=1}^{J}\left|\tilde{P}^o_{h_i}(y_j) - \tilde{P}^c_{h_i}(y_j)\right|}{\sum_{j=1}^{J}\tilde{P}^z_{h_i}(y_j)}\,\theta\left(x,\tilde{P}^o_{h_i}(y_j)\right) \tag{19}$$

$$\text{with } \theta(x,t) = \begin{cases} 1 \text{ for } P_{\mathbf{h}_i}(\mathbf{y}_j) > x \\ 0 \text{ for } P_{\mathbf{h}_i}(\mathbf{y}_j) \le x \end{cases}$$

These individual factors help to detect if some pole figures are particularly badly reproduced after the refinement.

Another type is the averaged relative deviation factors:

$$\overline{RP}_x^z = \frac{1}{I}\sum_{i=1}^{I} RP_x^z(h_i) \tag{20}$$

These are simply the arithmetic average of the previous ones. They help in comparing results on different samples. The global relative deviation factors are similar, but the averaging scheme differs:

$$RP_x^z = \frac{\sum_{i=1}^{I}\sum_{j=1}^{J}\left|\tilde{P}_{h_i}^o(y_j) - \tilde{P}_{h_i}^c(y_j)\right|}{\sum_{i=1}^{I}\sum_{j=1}^{J}\tilde{P}_{h_i}^z(y_j)}\,\theta\left(x,\tilde{P}_{h_i}^o(y_j)\right) \tag{21}$$

The Rietveld-like R-factors or "intensity-weighted", which take into account the normal Gaussian distribution standard deviation for each measured intensity, show less overall variation with the texture strength. It is a better indicator of the OD refinement reliability when comparing different samples. The individual weighted standard deviation factors are defined as:

$$Rw_x^z(h_i) = \frac{\sum_{j=1}^{J}\left[w_{ij}^o I_{h_i}^o(y_j) - w_{ij}^c I_{h_i}^c(y_j)\right]^2}{\sum_{j=1}^{J} w_{ij}^z {I_{h_i}^z}^2(y_j)}\,\theta\left(x,\tilde{P}_{h_i}^o(y_j)\right) \tag{22}$$

whose averaged factor is:

$$\overline{Rw}_x^z = \frac{1}{I}\sum_{i=1}^{I} Rw_x^z(h_i) \tag{23}$$

The global weighted standard deviation factors will be:

$$Rw_x^z = \frac{\sum_{i=1}^{I}\sum_{j=1}^{J}\left[w_{ij}^o I_{h_i}^o(y_j) - w_{ij}^c I_{h_i}^c(y_j)\right]^2}{\sum_{i=1}^{I}\sum_{j=1}^{J} w_{ij}^z {I_{h_i}^z}^2(y_j)}\,\theta\left(x,\tilde{P}_{h_i}^o(y_j)\right) \tag{24}$$

with $I^{z}_{h_i}(y_j) = \tilde{P}^{z}_{h_i}(y_j).N_{h_i}$ (Diffracted intensity)

N_{h_i} (Refined normalizing factor)

$$w^{z}_{ij} = \frac{1}{\sqrt{I^{z}_{h_i}(y_j)}}$$ (Diffracted intensity weight)

8.3.1.3 Quantitative Texture Analysis Software Programs

Several software programs may be used to do all the calculations necessary for Quantitative Texture Analysis. POFINT [41] is a simple MS-DOS based program developed in Turbo-Pascal used for data reduction and defocusing corrections in the case of conventional texture analysis, prior to the OD refinement. Beartex [42], one of the most used texture software, allows the refinement of the OD from the results obtained with point detectors. It has implemented also the calculation and representation of recalculated and inverse pole figures from the OD, and the deduction of the macroscopic elastic tensor of the textured material from the values of the coefficients of a single crystal, using the OD as a weight factor. The combined analysis methodology is implemented in a user-friendly interface: Materials Analysis Using Diffraction (MAUD) [43]. All the examples shown in this chapter have been obtained using these programs.

8.3.2 OD Texture Strength Factors

Once f(g) is satisfactorily obtained, one can calculate factors that give an estimate of the texture strength. Caution should be taken here when comparing samples on the base of overall texture strength parameters. Samples should have the same crystal symmetry and exhibit similar texture components.

The first texture strength parameter is the so-called 'texture index' [23] (expressed in m.r.d.^{2} units):

$$F^2 = \frac{1}{8\pi^2}\sum_i \left[f(g_i)\right]^2 \Delta g_i \qquad (25)$$

with $\Delta g_i = \sin\beta_i \Delta\beta\, \Delta\alpha\, \Delta\gamma$ is the OD cell volume.

This index varies from 1 (random powder) to infinity (perfect texture or single crystal). It represents the mean square value of the OD. Since this index is expressed in units that are not homogeneous with the distribution density units

(m.r.d.), to help comparison and interpretations, it is more convenient to compare the square roots of these values, *i.e.* the Texture Strength:

$$F = \sqrt{F^2} \tag{26}$$

The second overall texture strength parameter is a measure of the texture disorder, evaluated by the calculation of the texture entropy:

$$S = \frac{1}{8\pi^2} \sum_i f(g_i) \ln f(g_i) \Delta g_i \tag{27}$$

8.3.2.1 Characterization of the Randomly Oriented Volume Fraction

A sample exhibiting randomly oriented crystallites has an OD with 1 m.r.d. distribution densities for all g values. However, in some samples only a fraction of the total volume is randomly oriented, V_r, the rest, $V_c(g)$, being the oriented fraction volume having the orientation component or components, $f_c(g)$. The random part produces a "background" level in the OD, sometimes called "FON" or "PHON". The OD can be then expressed as:

$$f(g) = f_r + f_c(g) \tag{28}$$

with the mandatory condition $0 \le f_r \le 1$.

By integrating equation 12, taking into account equation 28:

$$\frac{1}{V} \oint [V_r + V_c(g)] \, dV(g) = \frac{1}{8\pi^2} \oint [f_r + f_c(g)] \, dg \tag{29}$$

which verifies after identification: $V_r/V = f_r$ for the random part, and

$$\frac{dV_c(g)}{V} = \frac{1}{8\pi^2} f_c(g) \, dg$$

for the textured part

Therefore, the minimum value of the OD, f_r, corresponds to the volume fraction of the material that is randomly oriented.

8.3.3 Estimation of the Elastic Properties of Polycrystals Using the Orientation Distributions

The OD calculated can be used to estimate the elastic properties of an oriented polycrystal from the values of the single crystal. We will now describe how one may use a geometric average of the tensor quantities to calculate an OD-weighted $C_{ijk\ell}^{M}$, in the case of single-phase materials. Such macroscopic stiffness can be used for example in the calculation of elastic waves propagation in surface acoustic wave devices.

8.3.3.1 Tensor Average

The volume average of a tensor quantity T, which varies inside the volume V can be calculated by:

$$\langle \mathsf{T} \rangle = \frac{1}{V} \int_{\mathrm{V}} \mathsf{T}\, dV \tag{30}$$

In general, tensors are considered constant inside individual grains, and the previous equation can be rewritten as:

$$\langle \mathsf{T} \rangle = \frac{1}{V} \sum_{i} \mathsf{T}\, \mathrm{V_i} \tag{31}$$

for which V_i/V represents the volume fraction or weight associated to each grain in the volume. Since tensor properties of a polycrystal depend on the crystal orientations, this has to be taken into account in the calculations. This can be done through the Orientation Distribution f(g):

$$\langle \mathsf{T} \rangle = \int_{\mathrm{g}} \mathsf{T}(\mathrm{g})\, \mathrm{f}(\mathrm{g})\, dg \tag{32}$$

where g varies in all the orientation space *G*.

It is important to note that using such arithmetic averaging procedures, the average of the inverse of the tensor is in general not equivalent to the inverse of the averaged tensor:

$$\left\langle \mathsf{T}^{-1} \right\rangle = \frac{1}{V} \sum_{i} \mathsf{T}^{-1} \; \mathrm{V_i} \neq \left\langle \mathsf{T} \right\rangle^{-1} \tag{33}$$

This is a problem if the tensor is aimed at representing a physical property, like the elastic tensor $C_{ijk\ell}$. If the average tensor is $C_{ijk\ell}^{M}$, the arithmetic average leads to $(C_{ijk\ell}^{M})^{-1} \neq S_{ijk\ell}^{M}$ that violates stress-strain equilibrium inside the polycrystal. Therefore, a different averaging procedure must be explored.

The geometric mean of a scalar is:

$$\lceil b \rceil = \prod_{k=1}^{N} b_k{}^{w_k} = \exp\left(\left\langle \ln b \right\rangle\right) \tag{34}$$

with $\left\langle \ln b \right\rangle = \sum_{k=1}^{N} \ln b_k w_k$

However, for a tensor the geometric mean is not straightforward. For the eigenvalues λ_I of a given matrix T, equation 34 can be rewritten as:

$$\lceil \lambda_I \rceil = \prod_{k=1}^{N} \lambda_k{}^{w_{i,k}} \tag{35}$$

which ensures that $\lceil \lambda_{I'} \rceil = 1/\lceil 1/\lambda_{I'} \rceil = \lceil \lambda_{I'}{}^{-1} \rceil^{-1}$. For the matrix T represented in its orthonormal basis of eigenvectors, it can be shown [44] that:

$$\lceil T \rceil_{ij'} = \exp(\langle \ln T \rangle_{i'j'}) = \exp(\langle \Theta \rangle_{ij,i'j'} \ln T_{i'j'}) \tag{36}$$

In this equation, Θ stands for the transformation applied to the tensor T that represents the property of a given single crystal of orientation g in the single crystal reference frame K_B, in order to bring it coincident to the sample reference frame K_A. Θ then depends on the tensor order, and its average is composed of elements $\langle \Theta \rangle_{ij}$ given by, similarly as in equation 32:

$$\left\langle \Theta \right\rangle_{ij,i'j'} = \int_{g} \Theta_i^{i'}(g) \Theta_j^{j'}(g) \, f(g) \, dg \tag{37}$$

8.3.3.2 Application to the Estimation of Elastic Properties

The modelling of the mechanical properties has concentrated most of the works of the studies of macroscopic anisotropic properties in geology and metallurgy. We will not describe here the Voigt and Reuss models that produce the lower and up-

per bounds of the macroscopic elastic coefficients, using arithmetic averaging. Hill developed later another model that derives from the two others [45]. Instead, we will focus on the geometric mean model. Due to the fact that we are dealing with real and symmetric tensors, the eigenvalues of the concerned tensors are real. But neither the $S_{ijk\ell}$ and $C_{ijk\ell}$ nor the s_{ij} and c_{ij} matrices are diagonal, and equation 36 cannot be used. It is necessary first to diagonalize them using an orthonormal basis of eigentensors $\mathbf{b}_{ij}^{(\lambda)}$, for instance in the case of the stiffness tensor $C_{ijk\ell}$ of eigenvalues $C^{(\lambda)}$:

$$((\mathbf{b}_{ij}^{(\lambda)})^{-1}\, C_{ijk\ell}\, \mathbf{b}_{k\ell}^{(\lambda)}) = C^{(\lambda)}\, \delta_{ij} \tag{38}$$

and

$$C_{ijk\ell} = \sum_{\lambda=1}^{6} C^{(\lambda)} \mathbf{b}_{ij}^{(\lambda)} \mathbf{b}_{k\ell}^{(\lambda)} \tag{39}$$

which extends to

$$\begin{aligned} (\ln C)_{ijk\ell} &= \sum_{\lambda=1}^{6} \ln(C^{(\lambda)}) \mathbf{b}_{ij}^{(\lambda)} \mathbf{b}_{k\ell}^{(\lambda)} \\ &= \ln\left[\prod_{\lambda=1}^{6} (C^{(\lambda)})^{\mathbf{b}_{ij}^{(\lambda)} \mathbf{b}_{k\ell}^{(\lambda)}} \right] \end{aligned} \tag{40}$$

Now applying the geometric average over orientations (equation 36), the macroscopic stiffness of the polycrystal can be calculated from:

$$C_{ijk\ell}^{M} = \lceil C \rceil_{ijk\ell} = \exp(\langle \ln C \rangle_{i'j'k'\ell'}) = \exp(\langle \Theta \rangle_{ijk\ell,i'j'k'\ell'} (\ln C)_{i'j'k'\ell'} \tag{41}$$

with

$$\langle \Theta \rangle_{ijk\ell,i'j'k'\ell'} = \int_{g} \Theta_{i}^{i'}(g) \Theta_{j}^{j'}(g) \Theta_{k}^{k'}(g) \Theta_{\ell}^{\ell'}(g)\, f(g)\, dg$$

and $(\ln C)B_{i'j'k'\ell'}$ is given by equation 40. However, before calculating the value $\lceil C \rceil B_{ijk\ell}$, one has to first diagonalize $\langle \ln C \rangle B_{i'j'k'\ell'}$ in order to extract the new eigenvalues and eigentensors for the oriented polycrystal. The four successive tensor transformations relate to the 4th order stiffness tensor character.

The factorial entering the calculation explains the term “geometric mean”, in the sense that the oriented polycrystal macroscopic stiffness is obtained by the mean averaging of the single crystal stiffness eigenvalues. Similar expressions may be obtained for the macroscopic compliance tensor $S_{ijk\ell}^{M}$, which admits as eigenvalues $S^{(\lambda)} = 1/C^{(\lambda)}$ the reciprocal of the stiffness eigenvalues. This ensures that the same macroscopic elastic properties are calculated when using stiffness or compliances. In other words, the average of the inverse macroscopic property is consistent with the inverse of the average macroscopic property. This may be the

reason why this modelling gives rather good estimates of the elastic properties [45], comparable to the ones obtained by more sophisticated models which require larger computation times.

As it is difficult to measure the effective elastic tensor of ferroelectric thin films, its calculation by a volume average of the elastic coefficients of the individual crystals is a good solution that allows, for example, analyzing the anisotropic character of this tensor, and the effect of texture on it. The application of this method to lead titanate-based films has been reported [46].

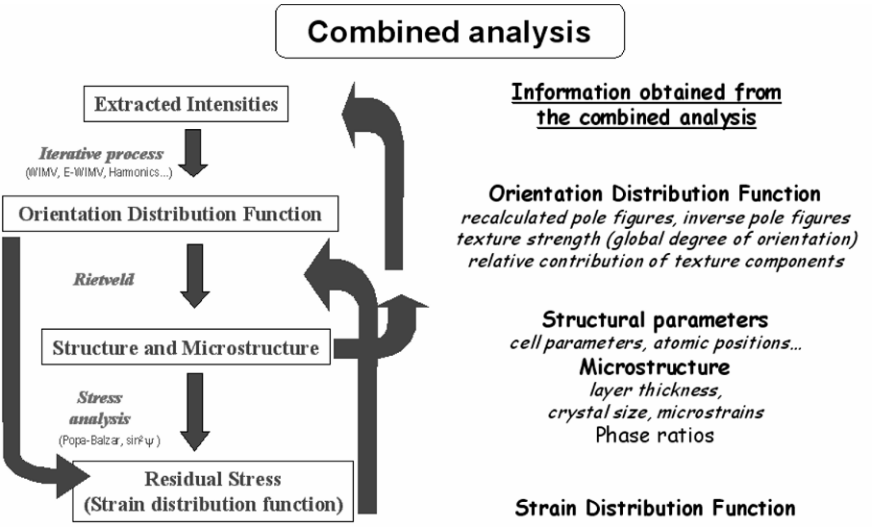

Fig. 8.24 Simplified diagram of the combined method of analysis of diffraction data. A list of the information that can be obtained and some of the algorithms implemented are also included.

8.4 Combined Analysis

Diffraction studies of materials are becoming more complex. Materials present an increasing level of complexity, for which we require as much information about the material characteristics as possible from a non-destructive technique. Heterostructures with several layers, materials with multiple phases, subjected to residual stress and textured are the present challenges for this kind of studies. For the determination of the structure, microsctructural parameters, residual stress and texture exists for each of them a particular method of analysis, which makes the whole characterisation a long and complex process. Furthermore, some parameters are not determined correctly without a precise determination of the others. This requires a global methodology of analysis of the diffraction data.

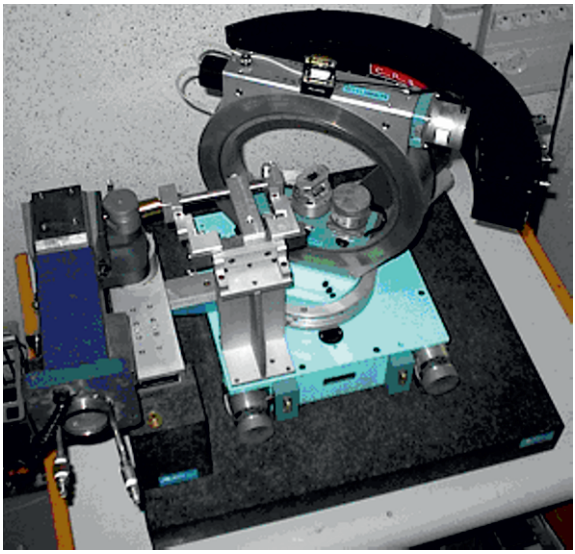

(a)

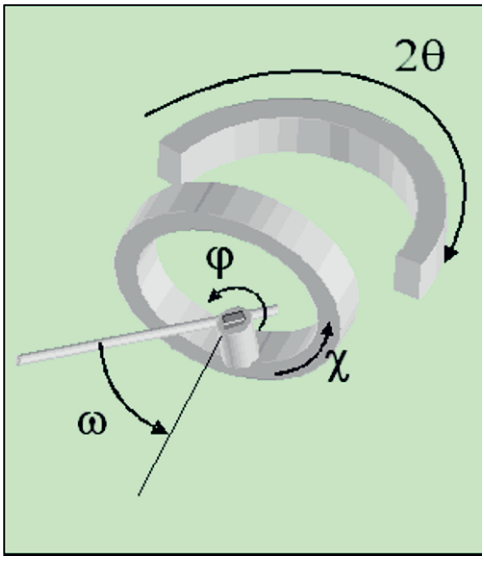

(b)

Fig. 8.25a Four-circle goniometer X-ray diffractometer equipped with a curved sensitive position detector. **b.** Schematic diagram showing the angle convention in a four-circle goniometer configuration.

A solution is the so-called combined analysis. This approach takes into account all the previous formalisms for texture, structure, microstructure, residual stresses, macroscopic elastic tensor and layering, by alternatively combining them in a single process. A first Rietveld refinement is operated in a cyclic manner on sets of diffraction diagrams measured at different sample orientations. Then, the extracted intensities are the input data for a Quantitative Texture Analysis cycle, the result of which is used to correct the diffraction intensities in the diagrams for the next Rietveld cycle. The result will be more reliable structural data and orientation distribution function. In between this process, a residual stress calculation of the polycrystal may be operated from the obtained OD. The operation leads to the determination of the parameters that produce the best solution for the whole ensemble of measurements.

Fig. 8.24 shows schematically the process of the combined analysis of diffraction data, the interdependency of the parameters accessible and the corresponding formalisms for refinement.The Materials Analysis Using Diffraction (MAUD) program [43] allows the use of the combined analysis of X-ray (conventional, synchrotron, monochromatic or energy dispersive, symmetric or asymmetric geometries, punctual, linear or planar detectors) and neutron (thermal, TOF) data.

8.4.1 Experimental Requirements for a Combined Analysis of Diffraction Data

The use of the combined analysis requires a large amount of diffraction data from the sample, which needs to be acquired using multiple detectors to avoid long measuring times. The first experiment allowing such an approach was developed using neutron data with a curved position sensitive (CPS) detector [47]. Using X-rays, the first experiment of this kind [35] used a CPS and a 4-circle diffractometer. Other studies follow, among them the characterization of thin ferroelectric structures [36–38, 39, 48].

Firstly, the diffractometer required for combined analysis must be equipped with a four circle goniometer in order to obtain reliable data for texture determination, *i.e.* at least one tilt rotation (χ), one azimuthal rotation (φ), an incidence angle (ω) and a detection circle (2θ), that can be a linear detector (Fig. 8.25).

The use of a curved position sensitive detector accelerates considerably the data acquisition as we can obtain for each (χ,φ) position a complete 2θ diffraction diagram (Fig. 8.26).

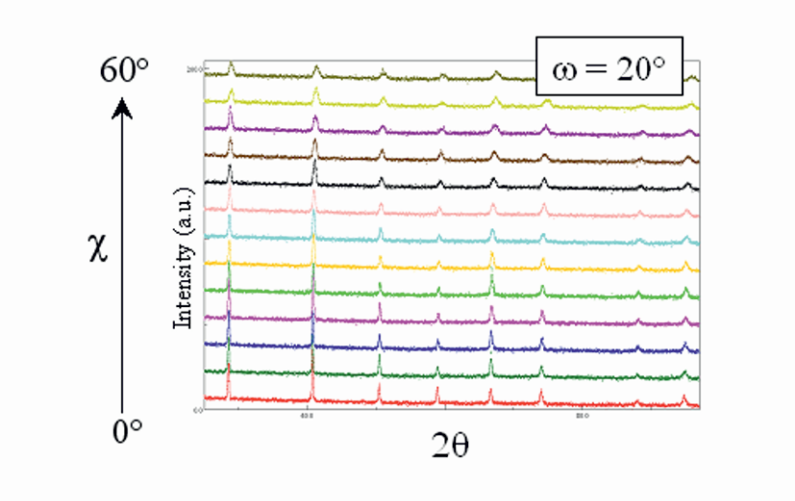

Fig. 8.26 Diffraction diagrams obtained with a diffractometer with a four-circle goniometer and a curve position sensitive detector.

8.4.2 Example of the Application of the Combined Analysis to the Study of a Ferroelectric Thin Film

A ferroelectric thin film of Ca-modified lead titanate of the nominal composition $Pb_{0.76}Ca_{0.24}TiO_3$ (PCT), was obtained by spin-coating deposition of a sol-gel processed solution on a $Pt/TiO_2/SiO_2/Si(100)$ substrate. The Pt layer on which the ferroelectric film is deposited on is a polycrystalline layer with <111> preferred orientation. The deposition of lead titanate based films on substrates with unrelated structures, i.e., without an obvious lattice match, as for this case, leads to a mixed orientation along <001> and <100> perpendicular to the film surface [49], which needs to be precisely characterized as it determines the ferroelectric behaviour of the films. In this tetragonal phase, the polar axis is along the <001> direction, which means that those crystallites oriented along <100> do not contribute to the net polarization of the film. From conventional quantitative texture analysis, we obtain that the films present a fibre-type texture (Fig. 8.27). But, the contributions of the two texture components cannot be determined accurately.

The PCT film texture is difficult to analyze due to the overlap of the diffraction peaks coming from the film and the substrate, and also of the 001 and 100 reflections from the PCT structure (Fig. 8.28). Integration in the conventional Quantitative Texture Analysis (QTA) is carried out over these two overlapped reflections, separating the <001> and <100> texture contributions during the WIMV iterative process [50, 51]. Besides, the information of those peaks overlapped with others

from the underlying layers of the substrate is not considered. This reduces considerably the input data used for the OD refinement. In the combined method the 001, 100 peaks are deconvoluted first using the Rietveld refinement. Then the E-WIMV process follows, and an improved evaluation of the texture is achieved. The real separation of the two texture components and the estimation of their contributions have only been possible by the use of this method [38]. This is true for any other material whose texture components are derived from directions whose reflections are close.

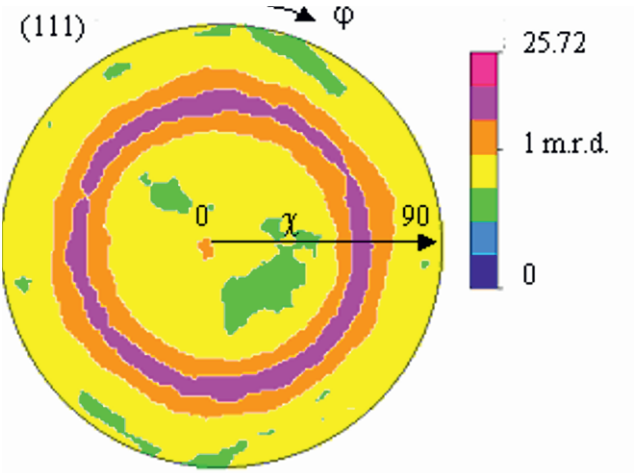

Fig. 8.27 PCT pole figure recalculated from the OD of a PCT/Pt/SiO2/(100)-Si thin structure that shows the fibre-type character of the texture. Equal area projection, logarithmic density scale.

Fig. 8.28 shows a selected series of X-ray diagrams measured at increasing tilt angles (every 5°), with their corresponding refinements using the combined method. It may be seen that all the diagrams are nicely reproduced, with reliability factors R_{Bragg} as low as 5 %. All this show the reliability of the refined values obtained with the combined method, not only for the ferroelectric film, but also for the Pt layer beneath it. The structural, microstructural and texture parameters obtained for both the PCT film and the Pt layer are summarized in Table 8.1 and Table 8.2.

Table 8.1 Structural, microstructural and texture parameters of the PCT and Pt layers obtained from the combined analysis of X-ray diffraction data (R_w = 7%; R_{Bragg} = 5%).

Layer	cell parameters (Å)	thickness (Å)	crystallite size (Å)	μ-strain (rms)	texture index (m.r.d.^{2})	RP_0 (%)
Pt	3.9108(1)	457(3)	458(3)	0.0032(1)	40.8	13.7
PCT	a = 3.9156(1) c = 4.0497(6)	4080(10)	390(7)	0.0067(1)	2.0	11.2

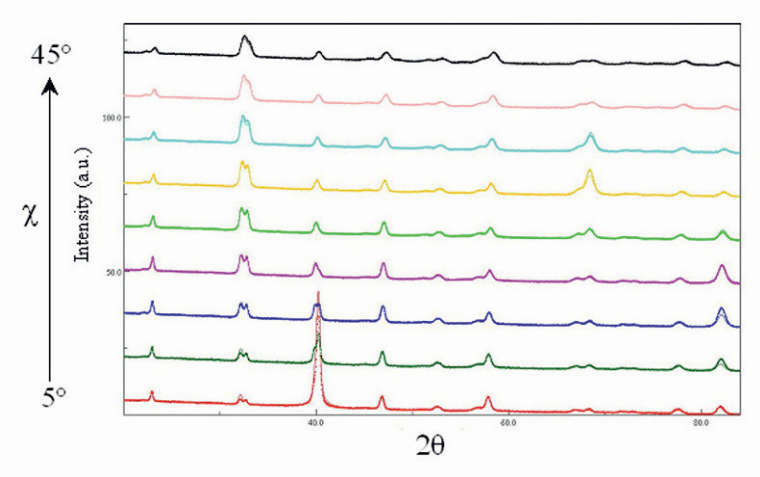

Fig. 8.28 Experimental X-ray diagrams for a PCT film (dotted line) and their corresponding refinement (solid line) obtained for tilted angles from $\chi = 5°$ to 45°.

Table 8.2 Refined structure of the PCT layer.

	Occupancy	x	y	z
Pb	0.76	0	0	0
Ca	0.24	0	0	0
Ti	1	0.5	0.5	0.477(2)
O1	1	0.5	0.5	0.060(2)
O2	1	0	0.5	0.631(1)

The lattice parameter obtained for the Pt is similar to the reported value by Swanson [52]: a = 3.9231 Å. But the ones corresponding to the PCT layer are not close to those reported previously for the same composition [53]: a=3.8939 Å and c=4.0496 Å. Although structural distortions may be present in the polycrystalline thin films, the possible explanation may be the stress state of these films. This difference in the cell parameters supports the idea that in the case of films deposited on a substrate, we should not rely in general on reported values but calculate them by the Rietveld method before starting a reliable texture analysis. The results of the microstructural parameters reveal the presence of larger microstrains in the PCT films than in the Pt layer, which presents the largest mean crystallite size. This is consistent with the fact that crystallites of the PCT film have sizes not larger than a tenth of the total layer thickness, while the Pt layer exhibits an average crystallite size that extends to the full thickness of the layer. The values obtained for the Pt and PCT layers thickness are close to the ones expected from the deposition conditions.

From the refined orientation distribution we can recalculate the pole figures (Fig. 8.29) for the PCT and Pt layers. Calculated texture indices are 2 mrd^2 for PCT and 41 mrd^2 for Pt. The texture of the Pt electrode is strong and characterized

by <111> directions perpendicular to the film plane as the only component. The ferroelectric PCT film has a preferential orientation component along <100> perpendicular to the film surface. Interestingly, no significant component along <001> is observed (Fig. 8.29) that contains the polar axis for this tetragonal phase. It must be noted that the conventional quantitative texture analysis gives similar estimated contributions for both directions, which shows the higher accuracy of the combined method.

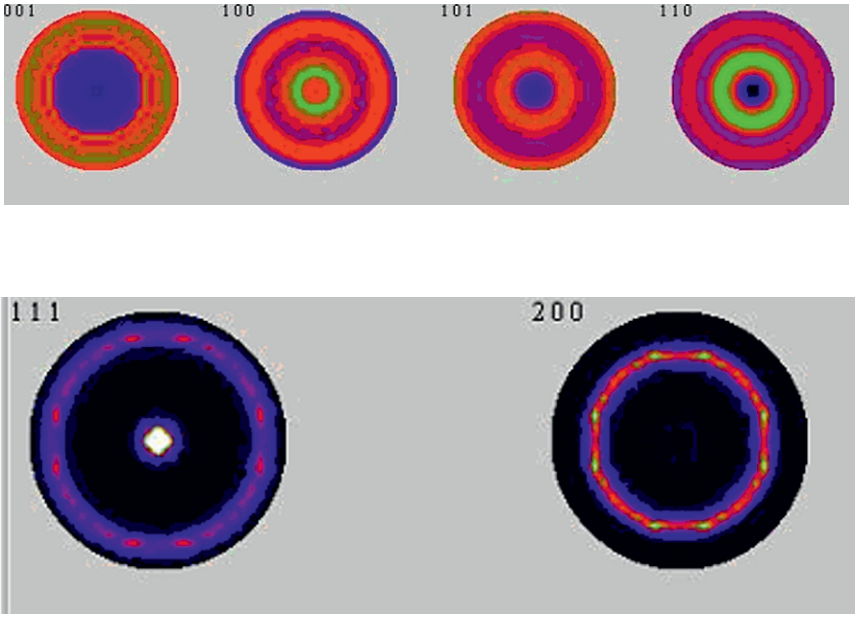

Fig. 8.29a. Recalculated pole figures for the PCT film. Equal area projections, linear density scale: 0.1-3.8 m.r.d.**b** Recalculated pole figures for the Pt layer. Equal area projections, logarithmic density scale: 0-63 m.r.d.

Compared to previous studies [50, 51], the approach appears to be far more powerful in extracting structural, microstructural and texture parameters in complex samples. Parameter divergence is astonishingly low, provided strongly dependent parameters were not released at the same time during the refinement process. This stability is probably due to the high number of experimental pole figures taken into account in the refinements, allowing a decrease of the defocusing effect (large at high χ-ranges) and a reduction of the number of possible OD solutions.

8.5 Texture of Polycrystalline Ferroelectric Films

8.5.1 Substrate Induced Texture Variations

The simplest approach to different textured films is the modification of the substrate on top of which the film is deposited. Silicon based substrates are important for the integration of these films with complementary metal oxide semiconductor (CMOS) technologies. Besides, ferroelectric films must be deposited on a conductive layer to be used in applications. Platinum is the most commonly used bottom electrode on Si-based substrates. But, to achieve the best properties of polycrystalline ferroelectric films, we need to have a preferential orientation out of the plane of the film that contains the polar axis. In this section, we will show how texture analysis helps to understand the effects of the modifications introduced in the substrate used.

8.5.1.1 Modifications of the Type of Substrate

We are interested in a film with a preferential orientation along its polar axis perpendicular to the films substrate for applications. In tetragonal perovskites, like lead titanate based compositions, polarization is along <001>. The problem is that this orientation is always associated to a similar one along <100>, i.e., with the polar axis in the plane of the film. Therefore, it does not contribute to the net polarization out of the plane of the film. This is because the crystallization takes place at the high temperature cubic phase, where the two directions are equivalent. Nevertheless, the presence of tensile or compressive stress during the cooling process may favour one of the two directions [54 55]. Among the possible origins of stress in films, the difference in the thermal expansion coefficients of the film and the substrate is one of them. Therefore, a change of the materials of the substrate may help tailor the contribution of the texture component along <001>. The results obtained by the use of different substrates are shown in Fig. 8.30. While the use of a Si-based substrate ($Pt/TiO_2/Si(100)$) produces a low textured PCT-Si film, the choice of Pt/MgO(100) or $Pt/SrTiO_3(100)$ instead of Si produces a stronger contribution of the <001> texture component, as the larger density values in the centre of the corresponding pole figure show. This is the consequence of the compressive stress developed in these films during crystallization. It is difficult to separate these two texture components, as there is an important overlap of their corresponding diffraction peaks. This is not possible to study with the conventional methods of analysis.

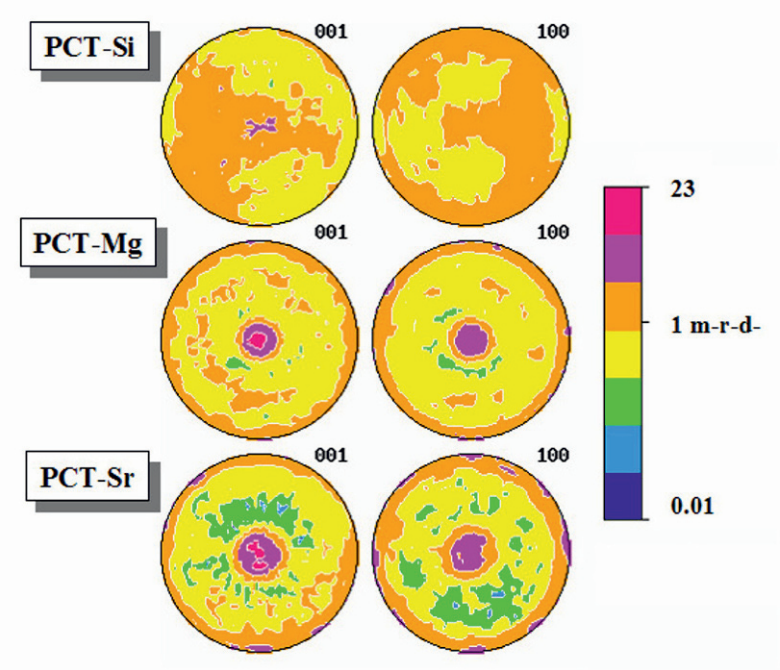

Fig. 8.30 Recalculated normalized pole figures for PCT films deposited on different substrates: $Pt/TiO_2/Si$ (PCT-Si); Pt/MgO (PCT-Mg); $Pt/SrTiO_3$ (PCT-Sr). Equal area projection and logarithmic density scale.

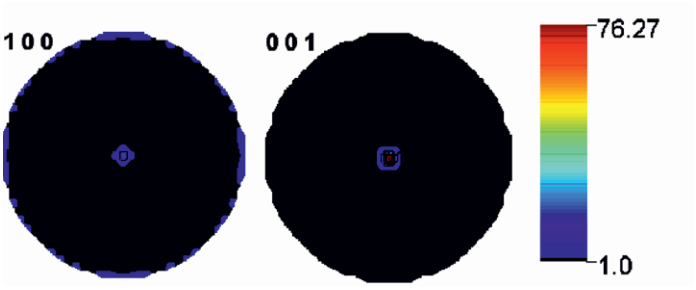

Fig. 8.31 Recalculated {100} and {001} pole figures of the PZT/Ti-Si film. Linear density scale, equal area projection.

It must be noted that the deposition of the ferroelectric film is on a polycrystalline Pt layer. Therefore, any significant change of its texture may be transferred to the film. The deposition of Pt on a Si-based substrate ($TiO_2/SiO_2/Si$) produces a fibre texture along <111>, but if it is on a MgO(100) under the right conditions the Pt film is oriented along <200>. To control the orientation of a $PbZr_{0.53}Ti_{0.47}O_3$ (PZT) film, a thin layer of TiO_x (2 nm) was deposited on top of the Pt before the ferroelectric film is prepared by radio frequency magnetron sputtering.

From the combined analysis, we obtain the pole figures shown in Figure 8.31 for the film deposited on the Si-based substrate (PZT/Ti-Si). Integration over the {001} and {100} poles shows that around 70% and 30% of the sample volume is oriented along <001> and <100> directions perpendicular to the sample surface, respectively. A similar orientation is found for the film deposited on the MgO-based substrate (PZT/Ti-MgO). Fig. 8.32 represents the evolution of the {001} and {100} distribution densities in function of the tilt angle χ. On this diagram, all intensities at every φ position have been summed for each χ and then normalized into distribution densities using direct normalization [56]. The film exhibits a high level of orientation with a maximum density at χ=0° around 1300 m.r.d. The most interesting feature of this graph is that it shows a non-negligible amount of crystallites with (100) planes nearly parallel to the sample plane (which in fact points around χ=2.5°). The existence of such slightly inclined (100) grains was reported earlier [57]- [58 59 60]. The disorientation angle of the (100) grains was shown to follow the expression $[2\tan^{-1}(c/a)]$-90° [60]. In our case where c/a = 1.07, this should lead to an angle of 3.9° for a fully relaxed thin film. As we measure an angle of 2.5°, this implies that some stress is remaining in the film. We determine a volume fraction of around 10% in volume for the undesired <100>-orientation component, lower than the one obtained for the PZT/Ti-Si film.

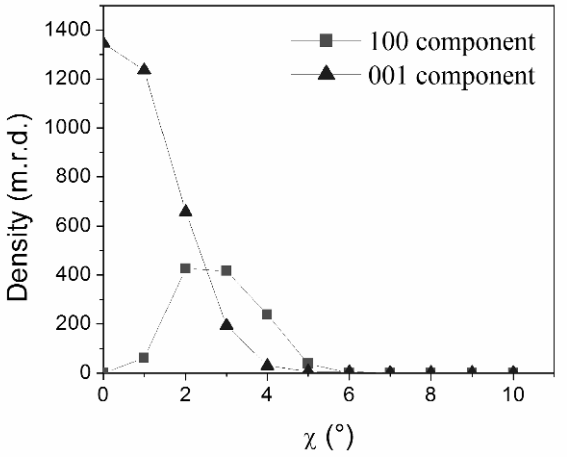

Fig. 8.32 {001} and {100} distribution density plot of the PZT/Ti-MgO film.

A change of the type of substrate may lead to the occurrence of some in-plane orientation contributions. $Pb(Zr_{0.6}Ti_{0.4})O_3$ films were obtained by RF sputtering [61] on a Si-based substrate: TiO_2/Pt(111)/TiO_2/SiO_2/Si(100) (PZT/Si); and on a $LaAlO_3$-based substrate: (TiO_2/Pt(111)/(012)$LaAlO_3$ (PZT-LAO). The TiO_2 layer is used to obtain in-situ crystallization and to promote growth along the <111> directions under previously determined conditions [7, 64, 65]. PZT-Si exhibits strong <111> fibre textures for the PZT and Pt layers, typical of the absence of

epitaxial relationship with the substrate. On the contrary, the PZT-LAO sample shows strong hetero-epitaxial relationships between PZT and Pt (Fig. 8.33). The {116}-LAO pole figure allows the determination of epitaxial relationships between LAO, Pt, and PZT. The four poles from the LAO single crystal R-plane allow the location of the $[110]_p$ perovskite-like directions in the equatorial plane using simple crystallography. The {220}-Pt pole figure shows 12 poles up to χ = 60° whereas a perfect single crystal would exhibit only three for this <111> orientation. This means four epitaxial relationships are equivalently present in the Pt film. As for {116}-LAO, intensity variations between the poles are only due to the large scan grid used compared to the pole dispersion. This latter effect is less pronounced for {220}-PZT, indicating that this phase is slightly more distributed than Pt. The four equivalents are explained by the matching possibilities generated between the 6 <110> directions of Pt in the sample plane and the $<110>_p$-LAO directions. The same epitaxial components are stabilized in the PZT layer. Table 8.3 compares the texture found in both films.

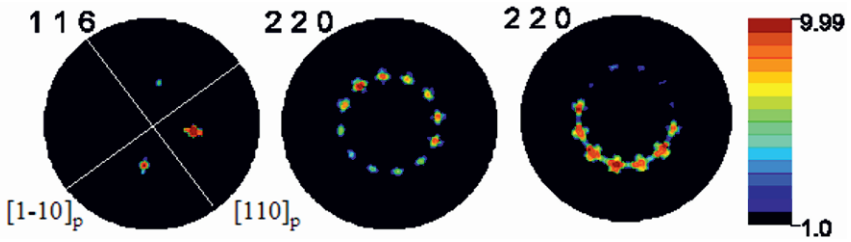

Fig. 8.33a {116}-LAO, **b** {220}-Pt, and **c)** $\{220\}_p$-PZT pole figures of the PZT-LAO film. $[hkl]_p$ state for a pseudo-cubic indexing. Equal-area projections, logarithmic density scale.

Table 8.3 Crystallographic hetero-epitaxial relationships between the substrate and the Pt layer, and between the Pt layer and PZT, out-of-plane and in-plane.

	substrate	Pt layer	PZT film
out-of-plane	$Si[100]/SiO_2$	Pt<111>	PZT<111>
in-plane	$Si[001]/SiO_2$	random	random
out-of-plane	$LaAlO_3$ [012]*	Pt<111>	PZT<111>
in-plane	[110]*	<110>	PZT<110>

The search for stronger orientations along specific crystallographic directions in ferroelectrics leads to the epitaxial growth on specific substrates. Rhombohedral Pb_2ScTaO_6 (PST) films were deposited by RF sputtering [64] onto a magnesium oxide buffer layer that had been deposited on a $(11\bar{2}0)$-Al_2O_3 single-crystal (PST/MgO-AlO) and onto a conventional $Pt/Ti/SiO_2/Si(100)$ (PST/Pt-Si). This sample exhibits strong preferred orientation along <100> perpendicular to the film surface as it may be seen in the pole figures of Fig. 8.34. A good agreement be-

tween experimental and recalculated pole figures may be observed, proving the high quality of the quantitative texture analysis. Pole figures show tetragonal symmetry, indicating a moderate in-plane orientation. This is corroborated by the calculated inverse pole figures (Fig. 8.35). The one corresponding to the normal direction Fig. 8.35a shows a preferential orientation along <100>. The strength of the PST in-plane alignment may be revealed by the maximum pole density in the other two inverse pole figures Fig. 8.35b and Fig. 8.35c, corresponding to the sample directions marked in Fig. 8.34 as I (parallel to $[10\bar{1}0]$-Al_2O_3 and [0001]-Al_2O_3) and II (at 45º from I), respectively. They show maxima of 5.5 m.r.d., less than a third of the density observed along the normal to the film surface (18.6 m.r.d.), along <100>-PST and <110>-PST with a broad girdle between the two.

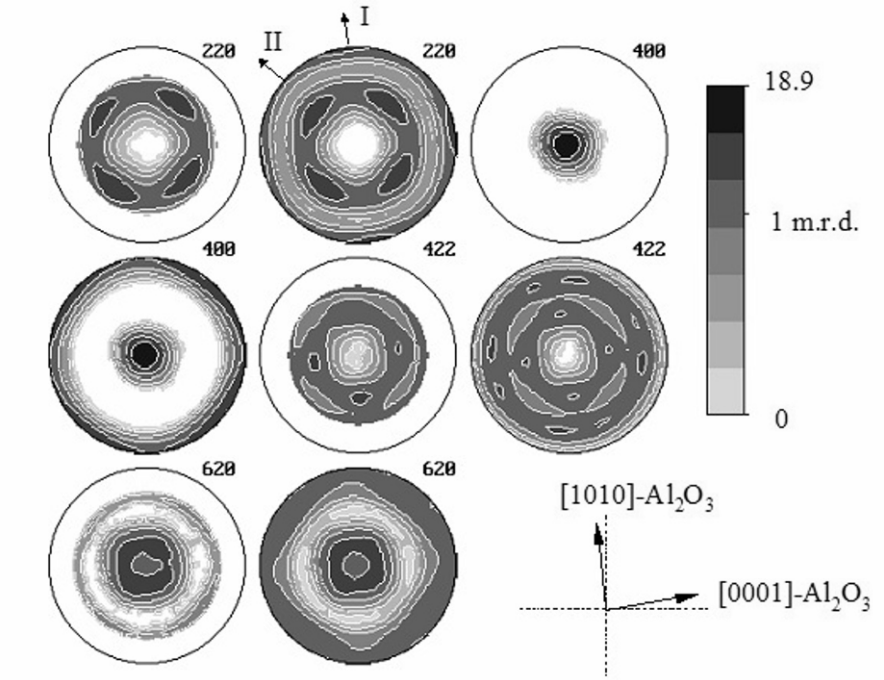

Fig. 8.34 Experimental and recalculated pole figures of film PST/MgO-AlO. Substrate in-plane parameters are indicated to identify the alignment. Equal area projection, logarithmic density scale.

The quantitative texture analysis of film PST/Pt-Si is also reliable as the agreement between recalculated and experimental pole figures of Fig. 8.36a shows. In this case, we obtain a strong preferred orientation along <111> direction at 5º from the normal of the film surface, but randomly distributed around this direction resulting in a fibre texture (Fig. 8.36a). The Pt layer shows also a <111> fibre texture tilted 5º respect to the film normal, which indicates the relation be-

tween these two layers. The inverse pole figure corresponding to the perpendicular to the film surface (Fig. 8.36b) corroborates that the only texture component of the PST film in this case is along <111>.

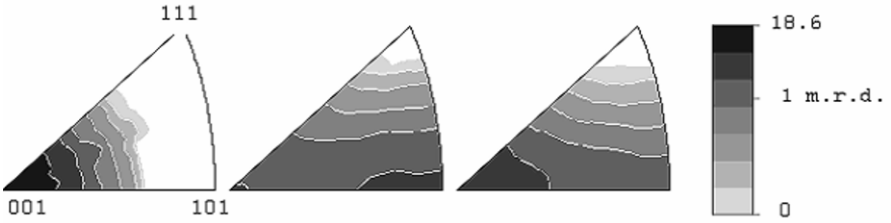

Fig. 8.35 Inverse pole figures of the film PST/MgO-AlO for: **a** direction perpendicular to the film surface, **b** direction I parallel to [100]-Al_2O_3 and **c** direction II at 45º from [100]-Al_2O_3 in the substrate plane. Equal area projection, logarithmic density scale, cubic sector.

The possible epitaxial relationships in film PST/MgO-AlO requires further study. The film was then aligned on the goniometer to have the **a** and **c** axes of the substrate ($[10\bar{1}0]$-Al_2O_3 and [0001]-Al_2O_3 directions respectively) approximately parallel to the vertical and horizontal pole figure axes (inset of Fig. 8.34). A subsequent texture analysis of the MgO layer reveals that the $<\bar{1}01>$-MgO directions align preferentially along the $[10\bar{1}0]$-Al_2O_3 and [0001]-Al_2O_3 axes of the substrate plane. This gives four statistically equivalent orientations with <111>-MgO tilted from the normal. We can deduce from the texture analysis that the major orientation relationships on this heterostructure are:

<100>-PST // ≈<111>-MgO // $[10\bar{2}0]$-Al_2O_3

<110>-PST // <211>-MgO and <110>-MgO // $[10\bar{1}0]$ and [000l]-Al_2O_3

The mismatch in d-spacings between d_{110}-PST and two d_{110}-MgO is 3.4%, and 0.4% between three d_{220}-PST and five d_{211}-MgO (Figure 8.37a). The mismatches between MgO and Al_2O_3 are larger and might explain the larger dispersion of the MgO texture. A first orientation (Fig. 8.37b) corresponds to coincidences of four d_{110}-MgO d-spacings with d_{001}-Al_2O_3 (8.3% of mismatch), and seven d_{211}-MgO with three d_{100}-Al_2O_3 and a mismatch of 2.6%. A second orientation (Figure 9.37c) is due to coincidences of three d_{220}-MgO d-spacings with d_{100}-Al_2O_3 (8.5% of mismatch), and eight d_{211}-MgO with d_{001}-Al_2O_3 with 5.9% of mismatch. Due to the weak mismatch differences between these two orientations, MgO crystallites may choose either orientation with an equal probability. This generates, associated with the fibre tilt, the four-fold symmetry of the texture pattern. Even if the texture of MgO is relatively weak, it produces a PST texture strength comparable to the one obtained for the film PST/Pt-Si, and allows the in-plane alignment of low-index crystallographic directions of PST.

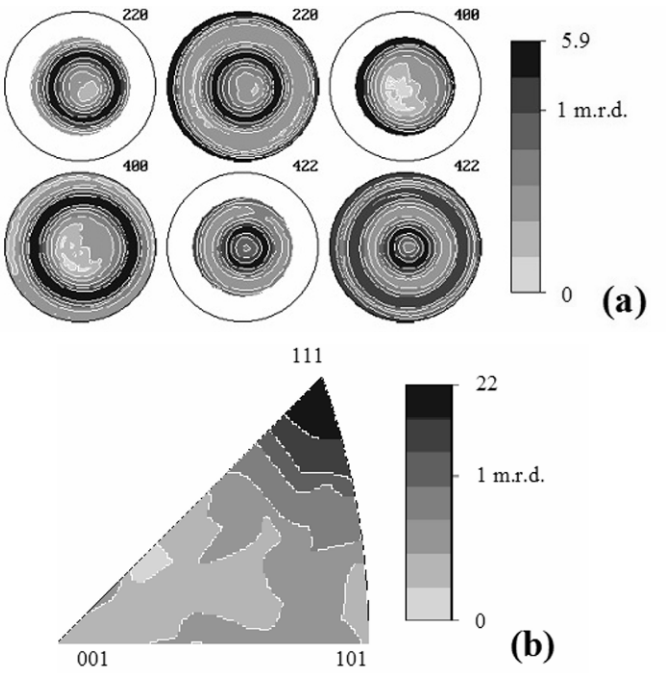

Fig. 8.36a Experimental and recalculated pole figures of the film PST/Pt-Si. **b** Inverse pole figure for the direction perpendicular to the film surface (cubic sector). Equal area projections, logarithmic density scales.

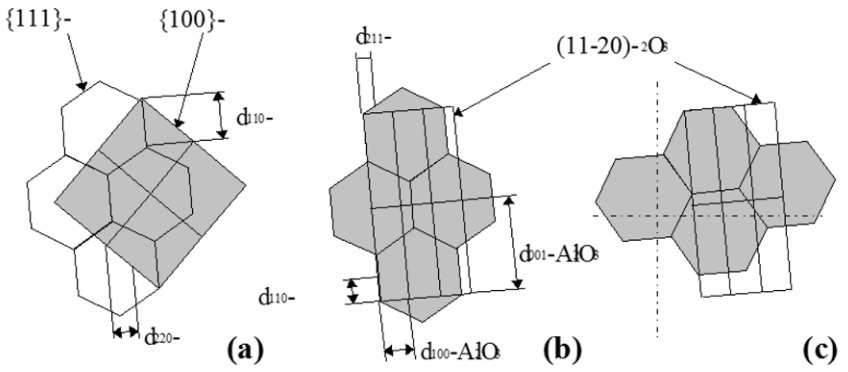

Fig. 8.37 Epitaxial relationships for film PST/MgO-AlO, as deduced from the quantitative texture analysis. Top layers are in gray shade: **a** {100}-PST planes on {111}-MgO, for one orientation of {111}-MgO; **b** first orientation of {111}-MgO plane on (11 $\bar{2}$ 0)-Al_2O_3; **c** second orientation of {111}-MgO planes on (11 $\bar{2}$ 0)-Al_2O_3.

The strategies to obtain the highest preferential orientation along the polarization axis in ferroelectrics sometimes include the choice of the right processing parameters. In the case of $LiNbO_3$ (LN) films, a two-step growth process was used which involves (1) creating a high-nucleation density by radio-frequency sputtering in the early stages of the film growth and (2) enhancing both the crystallinity and the texture by reactive chemical sputtering (also called pyrosol) [65]. The first weakly crystallized sputtered layer acts as a coherent buffer layer for the second pyrosol-layer, thus enhancing the desired texture strength and limiting chemical interfacial reactions. However, the substrate choice is determinant. The analysis of the texture of LN films deposited on Si(111) (LN/Si) and Al_2O_3(001) (LN/AlO) substrates results in a strong <001> preferential orientation [66]. In the LN film deposited on Si(111), the {100} pole figure (Fig. 8.38a) shows also <100> orientation, and the analysis of the {001} pole figure reveals that a ring centred at around 73° from the *c*-axes is a consequence of the occurrence of a <202> texture component. Similarly, in the analysis of the pole figures of the LN films deposited on the Al_2O_3(001) (Fig. 8.38b) we can see a slightly reinforced ring located at around 80° from the *c*-axes. It may be attributed to a texture component along <211>. For both films, the OD minimum is 0 indicating all the crystallites are orientated within the components. The texture index for LN/Si is F^2 = 9.7 m.r.d.^{2}, whereas for LN/AlO is 102 m.r.d.^{2}. This shows the strong hetero-epitaxial character of the texture in LN/AlO film. However, a single component of texture out-of-plane was achieved neither on Si nor on Al_2O_3 substrates. The main difference between the two heterostructures is in their in-plane orientation, as revealed by {100} pole figures (Fig. 8.38).

In the LN/Si film, all texture components are fibre-like (Fig. 8.38a). The film structure depends strongly on the initial growth stages. Crystallite orientation generally arises from either surface free energy or growth rate anisotropy [67]. LN is highly anisotropic and the c-axis is known to be one of the fastest growth directions. Then, after nucleation of the <001>-oriented grains, they grow preferably at the expense of other grain orientations. Besides, (111) planes of the fcc Si-substrate structure are highly dense, thus offering a large number of nucleation sites favourable for a dense and selected oriented growth. However, no coincidence site lattice with reasonable matching of the parameters could be identified between LN and Si. Therefore, there is no reason for ordering in the plane, resulting in an axially symmetric texture.

On the contrary, hetero-epitaxial-like textures are obtained on the <001>-Al_2O_3 substrate, with a d-spacing mismatch of 5 % ($d_{\{110\}}(Al_2O_3)$ = 0.258 nm; $d_{\{200\}}$(Si) = 0.271 nm), resulting in a stronger texture. Assuming a continuous oxygen sublattice at the interface between LN and Al_2O_3, the six-fold symmetry observed on the {100} pole figure (Fig. 8.38b) may be explained by two components of texture coming from differently aligned domains with different cation stacking sequences in each domain [68]. Each domain generates three-fold symmetry in the {100} pole figure, and is separated by 60° around the surface normal (namely $c_{\perp 0}$ being in exact alignment with the substrate and $c_{\perp 60}$). The

The intensities are approximately the same for the two stacking sequences and the film texture consist of two equally-distributed components with the following (1) and (2) hetero-epitaxial relationships:

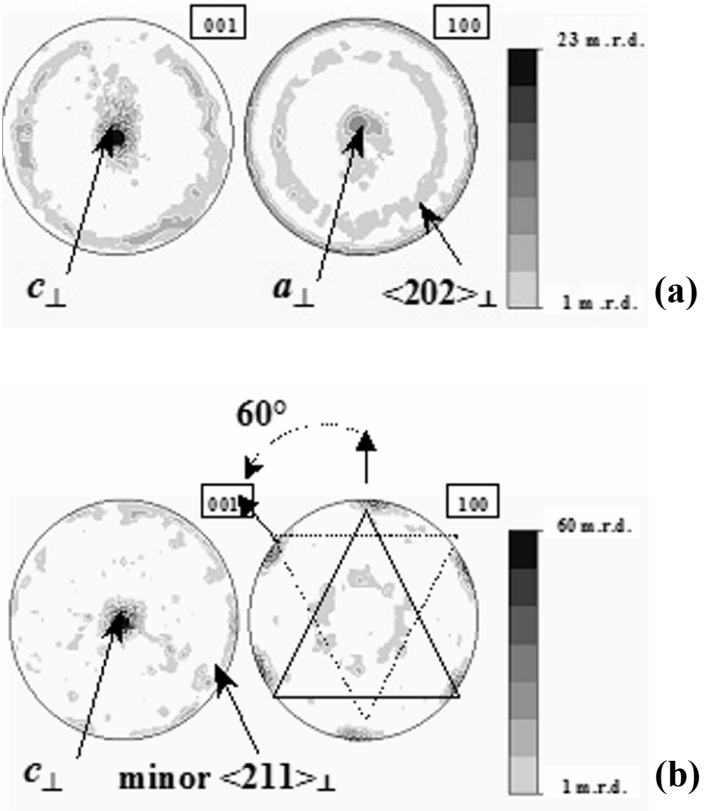

Fig. 8.38a Recalculated {001} and {100} pole figures of $LiNbO_3$ thin films deposited on Si(111) and **b** on Al_2O_3(001) substrates. Equal area projection, logarithmic scale.

($c_{\perp 0}$) <001> $LiNbO_3$ // <001> Al_2O_3 and <100> $LiNbO_3$ // <100> Al_2O_3 (1)
($c_{\perp 60}$) <001> $LiNbO_3$ // <001> Al_2O_3 and <110> $LiNbO_3$ // <100> Al_2O_3 (2)

Both (111)-Si and (001)-Al_2O_3 correspond to close-packed planes. Thus, when adsorbed on the surface of the substrates, the adatoms nucleate and form islands close-packed enough. This is to prevent their in-plane spread during the coalescence step by limiting the lateral growth rate and develop a columnar microstructure while keeping the same out-of-plane orientation (fastest growth direction perpendicular to the film surface). The presence of two in-plane variants in hetero-epitaxial $LiNbO_3$ films deposited onto Al_2O_3 substrates has already been observed and discussed by several authors. In particular, the 60° variant is thought to be partially strain/stress-driven and, therefore, influenced by the lattice mismatch between the two materials

[69]. Even though $LiNbO_3$ and α-Al_2O_3 are commonly indexed using the hexagonal notation, they are really trigonal (R3c and R-3c, respectively) and have only three-fold symmetry. The 60°-rotated grains can easily be shown to have a higher cation alignment ordering energy compared to the 120°-rotated grains because of the reduced distance between Al, Li and Nb at the interface [70]. However, if the adsorbed atoms or adsorbed molecules do not have a sufficient mobility to move far on the growth interface, they may be incorporated into an appropriate low energy site unless they arrive near it. Thus, the growth from these two different nuclei would result in two crystallographic variants in the films. However we explain the 50% observation for each orientation component alternative. It is by a more simple symmetry consideration giving rise to the presence of two texture components, consisting in crystallites having grown with their *c*-axes in opposite direction with respect to one another. In other words, the two crystallographic variants could be compared to parallel and anti-parallel domains, as synthesized.

As a conclusion, different types of substrates may be used to obtain different preferential orientations, sometimes using epitaxial growth. The effects may be studied thanks to the quantitative texture analysis. But, because microelectronic devices are based on Si, special attention must be paid to induce texture on films deposited on Si-based substrates. They may also be modified to obtain different preferential orientations in ferroelectric films.

8.5.1.2 Modifications of Si-Based Substrates

The Si-based substrates with a Pt electrode are normally $Pt/TiO_2/(100)Si$. Pt is the most commonly used bottom electrode due to its resistance to oxidation at the temperatures necessary for the film processing. As the ferroelectric film is deposited on top of this layer, modifications of Pt may lead to variations in texture of the film. One possibility is the increase of the surface roughness of the Pt layer resulting from an annealing process previous to film deposition. This will disrupt the usual nucleation process of the deposited film on the substrate. The inducement of preferential orientation in the lead titanate based films is along the <111> direction on those annealed substrates [71]. Conventional quantitative texture analysis does not give information on the Pt layer, because of the overlaps with the diffraction peaks coming from the ferroelectric film. But the use of the combined method allows the study of the evolution of the structure and texture of Pt before and after the annealing process (Table 8.4). The fibre type <111> orientation of this layer suffers an important increase of the texture index with the annealing process, as a consequence of a preferred growth of the <111> oriented crystals over the others. The $Pb_{0.76}Ca_{0.24}TiO_3$ film deposited on it, PCT-B, shows a decrease of the values of their cell parameters (refined with the combined analysis approach), while a <111> texture component becomes the most important in comparison with a film deposited onto a substrate without any pre-annealing, PCT-A (Table 8.4). This may be a consequence of the increase of the stress during the film formation on the rougher Pt surface.

Table 8.4 Structural and texture data of PCT films and Pt layers on substrates with and without an annealing at 650ºC previous to the film deposition.

	lattice parameters (Å)	texture index (m.r.d.)	main texture component
non-treated substrate			
Pt layer	a = 3.9108(1)	129	<111>
PCT-A film	a = 3.9156(1)	5.2	<100>
	c = 4.0497(6)		
annealed substrate			
Pt layer	a = 3.9100(4)	199	<111>
PCT-B film	a = 3.8920(6)	2.1	<111>
	c = 4.0187(8)		

The recalculated pole figures of the two PCT films deposited on untreated and annealed substrates (Fig. 8.39) show that a weak <111> texture component is already present in the PCT-A film deposited on an ordinary substrate. Its small contribution, together with the fact that the 111 reflection of PCT is close to the 111 of Pt, results in an underestimation of its contribution by conventional quantitative texture analysis. This means that this texture component had not been observed in previous studies [71]. Therefore, it seems that <111> becomes the most important texture component as the main <100> texture component does not appear in the annealed substrate. The decrease of the <100>-texture component results also in a decrease of the overall texture index.

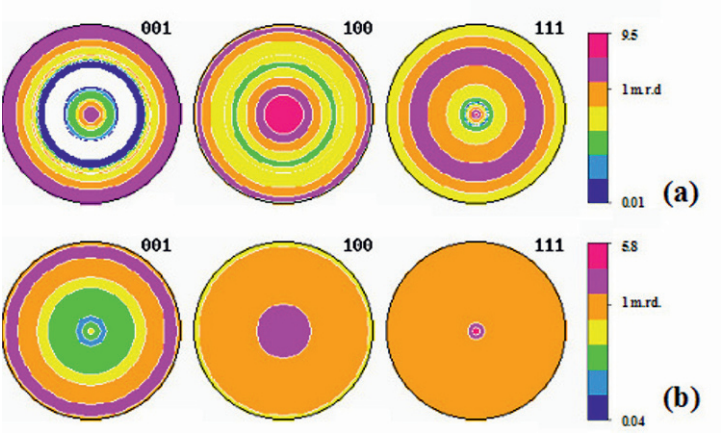

Fig. 8.39 Recalculated pole figures for PCT films deposited on **b** non-treated and **b** annealed at 650ºC $Pt/TiO_2/SiO_2/Si(100)$ substrates. Equal area projection and logarithmic density scale.

We can modify the substrate by adding an extra layer on top of the Pt layer to favour the growth of the grains along specific directions. The role of transient intermetallic layers, like Pt_xPb [72, 73], Pt_3Ti [74] and TiO_2 [75] have been reported to explain the occurrence of <111> preferential orientations of lead titanate based materials deposited on Pt layers.

To analyze the role of these intermetallic layers on texture using quantitative texture analysis, $Pb(Zr_{0.30}Ti_{0.70})O_3$ films were deposited by Chemical Solution Deposition methods on a normal Pt/Ti/Si(100) substrate (PZT-A) and on a Au/Pt/Ti/Si(000) (PZT-B). The Au layer will avoid the appearance of Pb, Pt or Ti-based intermetallics. OD calculations with low values of the reliability factors (RP0=20%; RP1=11%) showing the good quality of the refinement, reveal a reduction of the texture index from 32 m.r.d.^{2} (PZT-Pt) to 19 m.r.d.^{2} (PZT-Au). The {111} pole figures of both PZT (Fig. 8.40a) and Pt layers (not shown) present a strong maximum in their centre and random distributions of other axes around, characteristic of the <111> fibre textures. All OD minima for all layers are 0 m.r.d., indicating that all the material volume is textured within the components. The inverse pole figures of the PZT films for a direction perpendicular to the film surface (Fig. 8.40b) corroborate that the main texture component is the <111> fibre, although some minor orientation components along <110> and <100> can also be observed for PZT-Au.

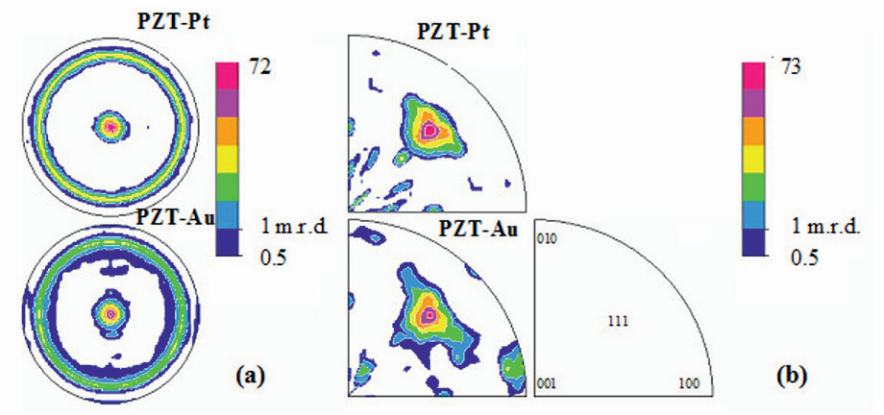

Fig. 8.40a Recalculated {111} pole figures of PZT thin films deposited on Pt/Ti/SiO_2/Si (PZT-Pt) and Au/Pt/Ti/SiO_2/Si (PZT-Au) substrates. **b** Inverse pole figures corresponding to a direction perpendicular to the film surface. Equal area projection, logarithmic density scale.

The use of an extra layer of Au on top of the Pt produces films less textured and containing the intermediate pyrochlore phase. The X-ray diffraction diagram of PZT-Au (not shown) suggests also less crystallinity than in the PZT-Pt film. The Au contributions are difficult to analyze, and reliable results are difficult to obtain. However, since Au crystallizes in an fcc crystal system with a cell parameter around 4.08 Å, we may expect this phase to follow approximately the Pt texture, though

with less orientation densities but still accommodating the <111> orientation of PZT. But it seems that Au stops the occurrence of intermetallic layers that promote the preferential orientation of lead titanate based films.

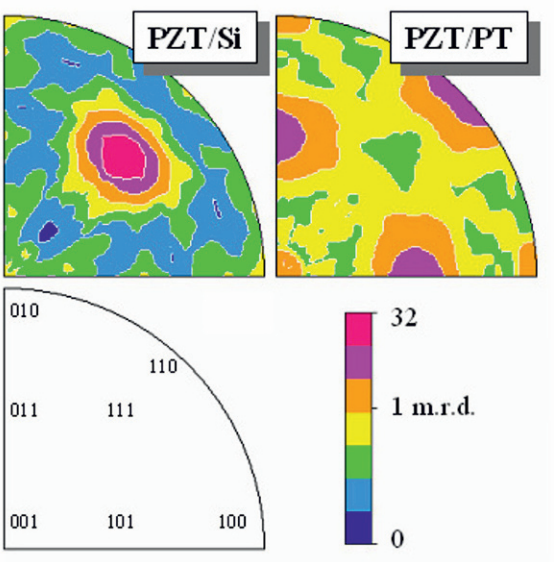

Fig. 8.41 Inverse pole figures corresponding to a direction perpendicular to the film surface of PZT films **a** deposited directly on a Si-based substrate (PZT/Si) and **b** on a $PbTiO_3$ layer (PZT/PT). Equal area projection, linear density scale.

A similar idea is explored with the use of a $PbTiO_3$ thin film between the ferroelectric film and the substrate. Rhombohedral $Pb(Zr_{0.54}Ti_{0.46})O_3$ (PZT films) of 420 nm thickness were deposited by sputtering directly on a Pt/Ti/Si(100) (PZT/Si) and on a 40 nm-thick $PbTiO_3$ layer (PZT/PT) [76]. The recalculated pole figures show that all the texture components are fibre-like, with their fibre axis along the sample normal. The inverse pole figures corresponding to that direction reveals all the orientation contributions (Fig. 8.41). It can be seen that the $PbTiO_3$ layer favours the occurrence of texture along <110> and <100> directions (F^2 = 2.5 m.r.d.^{2}), in contrast to the <111> preferential orientation without that layer (F^2 = 13 m.r.d.^{2}). Similarly, low reliability factors are obtained for the OD refinements (RP0: 15-26%; RP1: 10-13%).

Again, the introduction of a layer that stops the appearance of transient intermetallic layers between film and substrate disrupts the development of <111> textures. Instead, the crystals tend to nucleate on the surface of the $PbTiO_3$ on low energy planes of the high temperature cubic phase, like {001} and {110}. As a consequence, we obtain the texture components along <110> and <100> directions, but none along <111>, when the PZT film is deposited on a $PbTiO_3$ thin film.

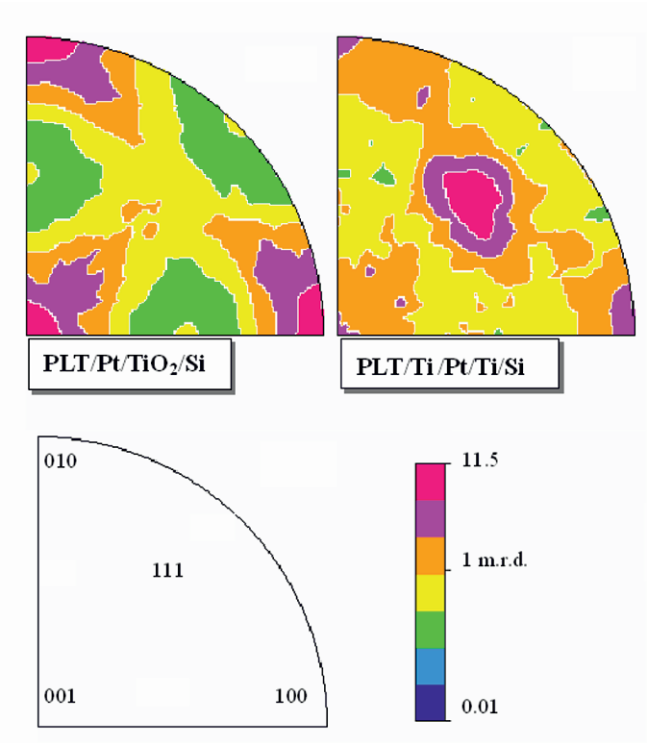

Fig. 8.42 Inverse pole figures corresponding to a direction perpendicular to the film surface for two PLT films deposited on Si-based substrates with and without a Ti layer. Equal area projection and logarithmic density scale.

It seems clear from previous studies [75, 77] that Ti containing layers play an important role in the inducement of <111> texture for lead titanate based thin films. However, none of them was able to clarify whether this orientation, although dominant, is the only one occurring. The results of the texture analysis of tetragonal $Pb_{0.88}La_{0.08}TiO_3$ (PLT) films deposited on a conventional Si-based substrate ($Pt/TiO_2/Si(100)$), and on a similar substrate but with an extra Ti layer (Ti/Pt/Ti/Si(100)), are shown in Fig. 8.42. The presence of the Ti layer produces a strong orientation along the <111> direction, as predicted, but preserving minor texture contributions along <001> and <100>. These contributions that account for 10 and 15 % of the oriented crystals, respectively, appear due to the nucleation of the $PbTiO_3$ perovskites on the low energy {100} planes of the high temperature cubic phase. Crystallization takes place in the cubic phase, and it seems those planes nucleate preferentially in the interface between film and substrate, even when there is no crystallographic relation with the substrate. Therefore, the "natural" orientation along <100>, <001> directions does not disappear when the <111> orientation is induced, but it becomes a small contribution that it is difficult to observe without a detailed analysis of texture.

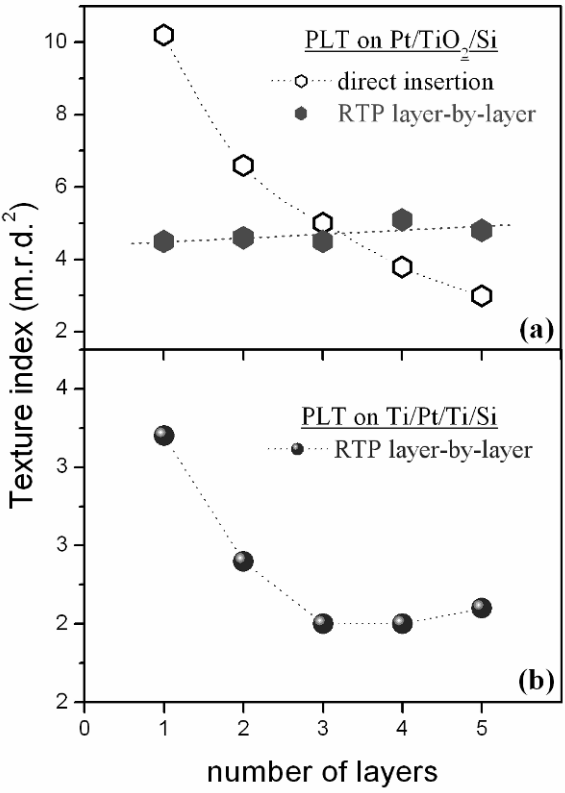

Fig. 8.43 Evolution of the texture index of PLT films with varying number of deposited layers: **a** crystallisation by direct insertion of the whole film in a furnace, and a layer-by-layer rapid thermal processing (RTP) of films deposited on $Pt/TiO_2/Si$; **b** layer-by-layer rapid thermal processing (RTP) of layers deposited on Ti/Pt/Ti/Si to induce <111> preferential orientation.

8.5.2 Influence of the Processing Parameters on the Development of Texture in Thin Films

The quantitative information on the texture of the films may be used to show tendencies that shed light onto the mechanisms involved in the development of preferential orientations, which can be closely related to their preparation process. This is shown in the study of $Pb_{0.88}La_{0.08}TiO_3$ (PLT) films prepared by chemical solution deposition methods with varying thickness [49]. An increasing number of deposited layers results in thicker films. Traditionally, the whole stack of deposited layers is crystallized in one step by direct insertion in a furnace. As we in-

crease the number of layers, we observe a decrease of the degree of orientation, i.e., the texture index. As this means a limitation of the film thickness to obtain highly textured films, we modify the crystallization by the so-called layer-by-layer process. This consists of the rapid thermal processing (RTP) of each layer before the following one is deposited. Variations of the texture index (Fig. 8.42a) of a maximum of 10% are obtained in this case, suppressing the thickness dependence of texture. In both cases, we obtained a mixed <100>, <001> orientation. No significant variations of the contributions of the texture components are observed. We conclude that the relative amount of crystals nucleated at the substrate-film interface with preferential orientation decreases as the film thickness increases. The layer-by-layer crystallization makes possible this kind of nucleation for each layer (this time on the layer-to-layer interface), and as a consequence the relative amount of oriented crystals remains almost constant as thickness increases. Of course, this is valid if the nucleation of oriented crystals takes place only on the interfaces between layers. In the case of induced <111> orientations by the introduction of an extra Ti layer on the substrate (Fig. 8.43b), texture index decreases with increasing number of deposited layers. This is because, in this case, nucleation of <111> oriented crystals is only occurring on the Ti layer. Therefore, the relative amount of these crystals decreases with increasing the thickness of the film. This is also clear looking at the values of <111> contribution to the texture. When the contribution of the <111> component is below ~50%, the texture of the film starts to be dominated by the <001> and <100> components. This means that the thickness effect on the texture disappears, and the value of the texture index reaches a stable value.

Final Remarks

Texture is an important issue for polycrystalline ferroelectrics as it determines their physical properties. The use of advanced methods of analysis of the diffraction data, namely the quantitative texture analysis or the combined method, allows access to quantitative information on the different components of the global texture and to more accurate structural parameters, not available by more conventional approaches. From the results obtained, important conclusions can be drawn regarding the mechanisms of development of preferred orientations and, also, the correlation between them and the ferroelectric behaviour. As these techniques are still evolving, improved and more reliable results are expected that will allow us to solve other problems in the characterization by diffraction of these complex structures.

Acknowledgements

We are indebted to many collaborators and organisations. We would like to thank L. Lutterotti (DIM-Trento), M. Morales (CIMAP-Caen), E. Guilmeau (CRISMAT-Caen) for their assistance in the application of the combined approach on several case studies. Most of this work would not have been possible without the ferroelectric films prepared by several research groups. We wish to thank M.L. Calzada, M. Algueró and R. Poyato (ICMM-CSIC Madrid) for the preparation of the PCT and PLT films; G. Leclerc, R. Bouregba and G. Poullain (CRISMAT-Caen) for the preparation of sputtered PZT films; R. Whatmore and Q. Zhang (Cranfield University) and A. Patel (GEC-Marconi) for providing PZT films obtained by spin-coating; V. Bornand (Univ. Montpellier) for the elaboration of the $LiNbO_3$ and $LiTaO_3$ films; and M. Todd (DRA Malvern) for the elaboration of PST films.

These studies have been funded over years through several projects and contracts. The European Union project ESQUI "X-ray Expert System for electronic films Quality Improvement" within the GROWTH program (G6RD-CT99-00169) deserves special mention as it provided an essential support to develop the tools used in the quantitative analysis of polycrystalline ferroelectrics that we show in this chapter.

References

1. Scott J.F. (2000) Ferroelectric Memories. Springer Series in Advanced Microelectronics 3, Springer-Verlag, Berlin-Heidelberg
2. Arimoto Y., Ishiwara H. (2004) Current status of ferroelectric random-access memory. MRS Bull. 29: 823-828
3. Muralt P., Baborowski J., Ledermann N. (2002) Chapter 12. Piezoelectre microelectromechanical-systems with $PbZr_xTi_{1-x}O_3$ thin films: Integration and application issues. In: N. Setter (Ed.) Piezoelectric Materials in Devices, EPFL Swiss Federal Institute of Technology, Lausanne, pp. 231-260
4. Wouters D.J., Willems G., Lee E.U., Maes H.E. (1997) Elucidation of the switching processes in tetragonal PZT by hysteresis loop and impedance analysis. Integr. Ferroelectr. 15:79-87
5. Jia C.L., Urban K., Hoffmann S., Waser R. (1998) Microstructure of columnar-grained $SrTiO_3$ and $BaTiO_3$ thin film prepared by chemical solution deposition. J. Mater. Res. 13:2206-2217
6. Kim S.-H., Park D.-Y., Woo H.-J., Lee D.-S., Ha J., Hwang C.S., Shim I.-B., Kingon A.I. (2002) Orientation effects in chemical solution derived $Pb(Zr_{0.3},Ti_{0.7})O_3$ thin films on ferroelectric properties. Thin Solid Films 416:264-270
7. Bouregba R., Poullain G., Vilquin B., Murray H. (2000) Orientation control of textured PZT thin films sputtered on silicon substrate with TiO_x seeding. Mater. Res. Bull. 35:1381-1390
8. Randle V., Engler O. (2000) Introduction to texture analysis. Macrotexture, microtexture and orientation mapping. CRC Press, Boca Raton, Florida

9. Brentano J.C.M. (1946) Parafocusing properties of microcrystalline powder layers in x-ray diffraction applied to the design of x-ray goniometers. J. Appl. Phys. 17:420-434
10. Wcislak L., Bunge H.J., Nauer-Gerhardt C.U. (1993) X-ray diffraction texture analysis with a position sensitive detector. Zeitschrift für Metallkunde 84: 479-493
11. Heizmann J.J., Laruelle C. (1986) Simultaneous measurement of several x-ray pole figures. J. App. Cryst. 19:467-472
12. Legrand C., Yi J.H., Thomas P., Guinebretière R., Mercurio J.-P. (1999) Structural characterisation of sol-gel $SrBi_2Nb_2O_9$ thin film deposited on (001) $SrTiO_3$ single crystal. J. Eur. Ceram. Soc. 19: 1379-1381
13. Lotgering F.K. (1959) Topotactical reactions with ferrimagnetic oxides having hexagonal crystal structures-I. J. Inorg. Nucl. Chem. 9:113-123
14. Jones J.L., Slamovich E.B., Bowman K.J. (2004) Critical evaluation of the Lotgering degree of orientation texture indicator. J. Mater. Res. 19: 3414-3422
15. Brosnan K.H., Messing G.L., Meyer Jr. R.J., Vaudin M.D. (2006) Texture measurements in <001> fiber oriented PMN-PT. J. Amer. Ceram. Soc. 89 1965-1971
16. O'Connor B.H., Li D.Y., Sitepu H. (1991) Strategies for preferred orientation corrections in x-ray powder diffraction using line intensity ratios. Advances in X-ray Analysis 34 409-415
17. Capkova P., Peschar R., Schenk H. (1993) Partial multiplicity factors for texture correction of cubic structures in the disc-shaped crystallite model. J. Appl. Cryst. 26:449-452
18. Cerny R, Valvoda V., Cladek M. (1995) Empirical texture corrections for asymmetric diffraction and inclined textures. J. Appl. Cryst. 28:247-253
19. O'Connor B.H., Li D.Y., Sitepu H. (1992) Texture characterization in x-ray powder diffraction using the March formula. /Advances in X-ray Analysis. Advances in X-ray Analysis 35:277-283
20. Pernet M., Chateigner D., Germi P., Dubourdieu C., Thomas O., Sénateur J.-P., Chambonnet D., Belouet C. (1994) Texture influence on critical current density of YBCO films deposited on (100)-MgO substrates. Physica C 235-240:627-628
21. Isaure M.-P., Laboudigue A., Manceau A., Sarret G., Tiffreau C., Trocellier P., Lamble G., Hazemann J.-L., Chateigner D. (2002) Quantitative Zn speciation in a contaminated dredgeg sediment by μ-PIXE, μ-EXAFS spectroscopy and principal component analysis. Geochimica et Cosmochimica Acta 66:1549-1567
22. Chateigner D., Hedegaard C., Wenk H.-R. (1996) Texture analysis of a gastropod shell: Cypraea testudinaria. In Z. Liang, L. Zuo, Y. Chu (eds.) 11th International Conference on Textures of Materials. Vol. 2. Int. Academic Publishers, pp. 1221-1226
23. Bunge H.J., Esling C. (eds) (1982) Quantitative Texture Analysis. DGM, Germany
24. Bunge H.J. (1982) Texture Analysis in Materials Science. P.R. Morris Trans., Butterworths, London
25. Matthies S. (1979) Reproducibility of the orientation distribution function of texture samples from pole figures (ghost phenomena). Physica Status Solidi B 92:K135-K138
26. Ruer D. (1976) Méthode vectorielle d'analyse de la texture. PhD thesis, Université de Metz, France
27. Vadon A. (1981) Généralisation et optimisation de la méthode vectorielle d'analyse de la texture. PhD thesis, Université de Metz, France
28. Schaeben H. (1988) Entropy optimization in quantitative texture analysis. J. Appl. Phys. 64:2236-2237
29. Helming K. (1998) Texture approximations by model components. Materials Structure 5:3-9
30. Pawlik K. (1993) Application of the ADC method for ODF approximation in cases of low crystal and sample symmetries. Mater. Sci. Forum 133-136:151-156
31. Williams R.O. (1968) Analytical methods for representing complex textures by biaxial pole figures. J. Appl. Phys. 39:4329-4335

32. Imhof J. (1982) The resolution of orientation space with reference to pole figure resolution. Textures and Microstructures 4:189-200
33. Matthies S., Vinel G.W. (1982) On the reproduction of the orientation distribution function of texturized samples from reduced pole figures using the conception of a conditional ghost correction. Physica Status Solidi B 112:K111-K114
34. Schaeben H. (1991) Determination of complete ODF using the maximum entropy method. In Bunge H.J., Esling C. (eds) Advances and applications of quantitative texture analysis. DGM, Oberursel, Germany, pp109-118
35. Cont L., Chateigner D., Lutterotti L., Ricote J., Calzada M.L., Mendiola J. (2002) Combined X-ray texture-structure-microstructure analysis applied to ferroelectric ultrastructures: a case study on $Pb_{0.76}Ca_{0.24}TiO_3$. Ferroelectrics 267:323-328
36. Morales M., Chateigner D., Lutterotti L., Ricote J. (2002) X-ray combined QTA using a CPS applied to a ferroelectric ultrastructure. Mater. Sci. Forum 408-412:1055-1060
37. Lutterotti L., Chateigner D., Ferrari S., Ricote J. (2004) Texture, residual stress and structural analysis of thin films using a combined X-ray analysis. Thin Solid Films 450:34-41
38. Ricote J., Chateigner D. (2004) Quantitative microstructural and texture characterization by X-ray diffraction of polycrystalline ferroelectric thin films. J. Appl. Cryst. 37:91-95
39. Ricote J., Chateigner D., Morales M., Calzada M.L., Wiemer C. (2004) Application of the X-ray combined analysis to the study of lead titanate based ferroelectric thin films. Thin Solid Films 450:128-133
40. Chateigner D. (2005) Reliability criteria in Quantitative Texture Analysis with Experimental and Simulated Orientation Distributions. J. Appl. Cryst. 38:603-611
41. Chateigner D. (2002) POFINT: a MS-DOS program for Pole Figure Interpretation. http://www.ecole.ensicaen.fr/~chateign/qta/pofint/
42. Wenk H.R., Matthies S., Donovan J., Chateigner D. (1998) BEARTEX: a Windows-based program system for quantitative texture analysis. J. Appl. Cryst. 31:262-269
43. Lutterotti L., Matthies S., Wenk H.-R. (1999). MAUD (Material Analysis Using Diffraction): a user friendly Java program for Rietveld texture analysis and more. National Research Council of Canada, Ottawa 1999, 1599-1604. http://www.ing.unitn.it/~luttero/maud/
44. Matthies S., Humbert M. (1995) The combination of thermal analysis and time-resolved X-ray techniques: a powerful method for materials characterization. J. Appl. Cryst. 28:31-42
45. Chateigner D. (ed) (2004) Combined analysis: structure-texture-microstructure-phase-stresses-reflectivity analysis by x-ray and neutron scattering. To appear ISTE. http://www.ecole.ensicaen.fr/~chateign/texture/combined.pdf
46. Ricote J., Chateigner D., Algueró M. (2005) Intrinsic effective elastic tensor of ferroelectric polycrystalline lead titanate based thin films with fiber-type texture.Thin Solid Films 491:137-142
47. Chateigner D., Lutterotti L., Hansen T. (1998) Quantitative phase and texture analysis on ceramics-matrix composites using Rietveld texture analysis. ILL Highlights 1997 28-29
48. Lutterotti L., Matthies S., Chateigner D., Ferrari S., Ricote J. (2002) Rietveld texture and stress analysis of thin films by X-ray diffraction. Mater. Sci. Forum 408-412:1603-1608
49. Ricote J., Poyato R., Algueró M., Pardo L., Calzada M.L., Chateigner D. (2003) Texture development in modified lead titanate thin films obtained by chemical solution deposition on silicon-based substrates. J. Am. Ceram. Soc. 86:1571-1577
50. Ricote J., Chateigner D. (1999) Quantitative texture analysis applied to the study of preferential orientations in ferroelectric thin films. Bol. Soc. Esp. Cerám. Vidrio. 38:587-591

51. Ricote J., Chateigner D., Pardo L., Algueró M., Mendiola J., Calzada M.L. (2000) Quantitative analysis of preferential orientation components of ferroelectric thin films. Ferroelectrics 241:167-174
52. Swanson T (1953). Natl. Bur. Stand. (U.S.), Circ. 539, I, 31. (JCPDS file 04-0802)
53. Mendiola J., Jiménez B., Alemany C., Pardo L.,. Del Olmo L. (1989) Influence of calcium on the ferroelectricity of modified lead titanate ceramics. Ferroelectrics 94:183-188
54. Foster C.M., Li Z., Buckett M., Miller D., Baldo P.M., Rhen L.E. Bai G.R., Guo D., You H., Merkle K.L. (1995) Substrate effects on the structure of epitaxial $PbTiO_3$ films prepared on MgO, $LaAlO_3$ and $SrTiO_3$ by metalorganic chemical-vapor deposition. J. Appl. Phys. 78:2607-2622
55. Ricote J., Chateigner D., Calzada M.L., Mendiola J. (2002) Preferential orientation of ferroelectric calcium modified lead titanate thin films grown on various substrates. Bol. Soc. Esp. Cerám. Vidrio 41:80-84
56. Guilmeau E., Funahashi R., Mikami M., Chong K., Chateigner D. (2004) Thermoelectric properties–texture relationship in highly oriented $Ca_3Co_4O_9$ composites. Appl. Phys. Lett. 85 :1490-1492
57. Foster C.M., Li S., Buckett M., Miller D., Baldo P.M., Rhen L.E., Bai G.R., Guo D., You H., Merkle K.L. (1995) Substrate effects on the structure of epitaxial $PbTiO_3$ thin films prepared on MgO, $LaAlO_3$, and $SrTiO_3$ by metalorganic chemical-vapour deposition. J. Appl. Phys. 78:2607-2622
58. Hsu W.Y., Raj R. (1995) X-ray characterization of the domain structure of epitaxial lead titanate thin films on (001) strontium titanate. Appl. Phys. Lett. 67:792-794
59. Foster C.M., Pompe W., Daykin A.C., Speck J.S. (1995) Relative coherency strain and phase transformation history in epitaxial ferroelectric thin films. J. Appl. Phys. 79:1405-1415
60. Speck J.S., Daykin A.C., Seifert A. (1995) Domain configurations due to multiple misfit relaxation mechanisms in epitaxial ferroelectric thin films. III. Interfacial defects and domain misorientations. J. Appl. Phys. 78:1696-1706
61. Leclerc G., Poullain G., Bouregba R., Chateigner D. (2008) Influence of the substrate on ferroelectric properties of <111> oriented $Pb(Zr_{0.6}T_{0.4})O_3$ thin films. Appl. Surf. Sci. 255:4293
62. Vilquin B., Le Rhun G., Bouregba R., Poullain G., Murray H. (2002) Effect of in situ Pt bottom electrode deposition and of Pt top electrode preparation on PZT thin films properties. Appl. Surf. Sci. 195:63-73
63. Leclerc G., Domenges B., Poullain G., Bouregba R. (2006) Elaboration of (111)-oriented La-doped PZT thin films on platinized silicon substrates. Appl. Surf. Sci. 253:1143-1149
64. Huang Z., Todd M.A., Watton R., Whatmore R.W. (1998) Sputtered lead scandium tantalite thin films: a microstructural study. J. Mater. Sci. 33:363-370
65. Bornand V., Chateigner D., Papet P., Philippot E. (1997). Piezoelectric thin films obtained by pyrosol process. Ann. Chim. Sci. Mat. 22: 683-686
66. Bornand V., Huet I., Chateigner D., Papet Ph. (2002) Oriented Growth of $LiNbO_3$ Thin Films for SAW properties. Mater. Sci. Forum 408-412:1573-1578
67. Smith D.L. (1995) Thin film deposition principles and practice. McGraw Hill, New York, pp. 327-380
68. Fork D.K., Armani-Leplingard F., Kingston J.J., Anderson G.B. (1985) Thin Film Epitaxial. Oxide Optical Waveguides. Mater. Res. Symp. Proc. 392:189-200
69. Derouin T.A., Lakeman C.D.E., Wu X.H., Speck J.S., Lange F.F. (1997) Effect of lattice mismatch on the epitaxy of sol-gel $LiNbO_3$ thin films. J. Mater. Res. 12:1391-1400
70. Guo J., Ellis D.E., Lam D.J. (1992) Electronic structure and energetics of sapphire (0001) and (1-102) surfaces. Phys. Rev. B 45:13647-13656

71. Ricote J., Morales M., Calzada M.L. (2002) Texture analysis of ferroelectric thin films on platinized Si-based substrates with a TiO_2 layer. Mater. Sci. Forum 408-412:1543-1548
72. S.Y. Chen and I.W. Chen (1994) Temperature-time texture transition of $Pb(Zr_{1-x}Ti_x)O_3$ thin films: I. Role of Pb-rich intermediate phases. J. Am. Ceram. Soc. 77:2332-2336
73. Z. Huang, Q. Zhang and R.W. Whatmore (1999) Structural development in the early stages of annealing of sol-gel prepared lead zirconate titanate thin films. J. Appl. Phys. 86:1662-69
74. Y. Liu and P.P. Phulé (1996) Nucleation- or growth-controlled orientation development in chemically derived ferroelectric lead zirconate titanate ($Pb(Zr_xTi_{1-x})O_3$, x=0.4) thin films. J. Am. Ceram. Soc. 79:495-98
75. Muralt P., Maeder T., Sagalowicz L., Hiboux S., Scalese S., Naumovic D., Agostino R.G., Xanthopoulos N., Mathieu H.J., Patthey L., Bullock E.L. (1998). Texture control of $PbTiO_3$ and $Pb(Zr,Ti)O_3$ thin films with TiO_2 seeding. J. Appl. Phys. 83:3835-3841
76. Cattan E., Velu G., Jaber B., Remiens D., Thierry B. (1997) Structure control of $Pb(Zr,Ti)O_3$ films using $PbTiO_3$ buffer layers produced by magnetron sputtering. Appl. Phys. Lett. 70:1718-1720
77. Calzada M.L., Poyato R., García López J., Respaldiza M.A., Ricote J., Pardo L. (2001) Effect of the substrate heterostructure on the texture of lanthanum modified lead titanate thin films. J. Eur. Ceram. Soc. 21:1529-1533